

# Deep Single Image Camera Calibration by Heatmap Regression to Recover Fisheye Images Under Manhattan World Assumption Without Ambiguity

Nobuhiko Wakai<sup>1</sup> Satoshi Sato<sup>1</sup> Yasunori Ishii<sup>1</sup> Takayoshi Yamashita<sup>2</sup>

<sup>1</sup> Panasonic Holdings <sup>2</sup> Chubu University

{wakai.nobuhio, sato.satoshi, ishii.yasunori}@jp.panasonic.com takayoshi@isc.chubu.ac.jp

## Abstract

In orthogonal world coordinates, a Manhattan world lying along cuboid buildings is widely useful for various computer vision tasks. However, the Manhattan world has much room for improvement because the origin of pan angles from an image is arbitrary, that is, four-fold rotational symmetric ambiguity of pan angles. To address this problem, we propose a definition for the pan-angle origin based on the directions of the roads with respect to a camera and the direction of travel. We propose a learning-based calibration method that uses heatmap regression to remove the ambiguity by each direction of labeled image coordinates, similar to pose estimation keypoints. Simultaneously, our two-branched network recovers the rotation and removes fisheye distortion from a general scene image. To alleviate the lack of vanishing points in images, we introduce auxiliary diagonal points that have the optimal 3D arrangement of spatial uniformity. Extensive experiments demonstrated that our method outperforms conventional methods on large-scale datasets and with off-the-shelf cameras.

## 1. Introduction

In city scenes, image-based recognition methods are widely used for cars, drones, and robots. It is desirable to recognize the directions in which roads exist for navigation, self-driving, and driver assistance. To avoid obstacles, it is important to detect cars and pedestrians in front of a vehicle rather than at the sides in Figure 1. We can obtain the direction of travel and camera pan angles from odometry, gyros, or accelerator sensors using these specific devices. By contrast, image-based angle estimation is easy to use and does not require such devices. However, pan angles in a Manhattan world [8] have four-fold rotational ( $90^\circ$ ) symmetric ambiguity. A Manhattan world defines orthogonal world coordinates along cuboid buildings, and the origin of a pan angle ( $0^\circ$ ) is arbitrary with respect to the four directions at a road intersection. Therefore, estimating pan angles without

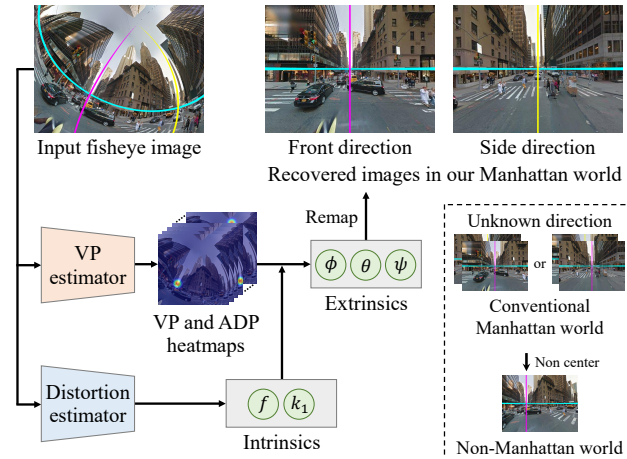


**Figure 1:** Our network predicts extrinsics and intrinsics in our Manhattan world from a single image. Our predicted camera parameters are used to fully recover images by remapping them while distinguishing the front and side directions. By contrast, the conventional Manhattan world cannot distinguish the origin of pan angles from a single image. Cyan, magenta, and yellow lines indicate the three orthogonal planes of our Manhattan frame in each of the images. The input image is generated from [32].

such ambiguity has remained an open challenge.

To control cars, drones, and robots, images for recognition are needed that have a large field of view (FOV). Fisheye cameras have a larger FOV than other cameras, but fisheye images are highly distorted. After fisheye distortion has been removed, various learning-based recognition methods, such as object detection [19, 21], semantic segmentation [6, 20], lane detection [55], action recognition [44, 51], and action prediction [15] can be used. To recover fisheye images, it is best to perform camera calibration before the recognition tasks mentioned above.

Geometry-based calibration methods can estimate the camera rotation and distortion from a distorted image [2, 25, 35, 49]. However, it is difficult for geometry-based methods to calibrate cameras from images that contain few artificial objects because these methods need to detect many

**Table 1:** Comparison of the features of conventional methods and our proposed method

Method	DL <sup>1</sup>	Heatmap <sup>1</sup>	Manhattan <sup>1</sup>	Pan	Unique pan <sup>2</sup>	Tilt & Roll	Dist <sup>2</sup>	>180° FOV <sup>2</sup>	Projection
Non-Manhattan world									
López-Antequera [26]	CVPR'19	✓				✓	✓		Perspective
Wakai [46]	ICCVW'21	✓				✓	✓	✓	Equisolid angle
Wakai [45]	ECCV'22	✓				✓	✓	✓	Generic camera [45]
Manhattan world									
Wildenauer [49]	BMVC'13		✓	✓		✓	✓		Division model [9]
Antunes [2]	CVPR'17		✓	✓		✓	✓		Division model [9]
Pritts [35]	CVPR'18		✓	✓		✓	✓		Division model [9]
Lochman [25]	WACV'21		✓	✓		✓	✓		Division model [9]
Ours		✓	✓	✓	✓	✓	✓ [45]	✓	Generic camera [45]

<sup>1</sup> DL is learning-based methods; Heatmap is heatmap regression; Manhattan is based on the Manhattan world for pan angles

<sup>2</sup> "Unique pan" is pan angles without four-fold rotational symmetric ambiguity; Dist is distortion; ">180° FOV" is supporting over 180° FOV

arcs to estimate the vanishing points (VPs). Therefore, city scenes that include sky or trees lining a street degrade the performance of geometry-based methods. In addition, their calibration accuracy has much room for improvement.

On the basis of the observations above, we define the origins of pan angles in a Manhattan world [8] to remove the pan-angle ambiguity. To achieve accurate and robust estimation, we propose a learning-based calibration method that predicts extrinsic parameters (pan, tilt, and roll angles), focal length, and a distortion coefficient simultaneously from a single image in Figure 1. Our heatmap regression predicts each direction using labeled image coordinates to distinguish the four directions of a road intersection in our Manhattan world. Furthermore, we introduce additional geometric keypoints, called auxiliary diagonal points (ADPs), to address the lack of VPs in each image.

To investigate the effectiveness of the proposed methods, we conducted extensive experiments on three large-scale datasets [5, 32, 57] and two subsets as well as off-the-shelf cameras. This evaluation demonstrated that our method notably outperforms conventional geometry-based [25, 35] and learning-based [26, 45, 46] methods. The major contributions of our study are summarized as follows:

- We propose a definition of pan angles in a Manhattan world. The definition is based on the directions of roads with respect to the camera location and the travel direction, and it removes pan-angle ambiguity. To the best of our knowledge, we are the first researchers to calibrate pan angles without four-fold rotational symmetric ambiguity from a general scene image.
- We propose a heatmap-based VP estimator for recovering the rotation from an image, to achieve higher accuracy and robustness than geometry-based methods using arc detectors.
- We introduce auxiliary diagonal points with an optimal 3D arrangement based on the spatial uniformity of regular octahedron groups, to address the ambiguity caused by the lack of VPs in an image.

## 2. Related work

**Manhattan world.** Coughlan *et al.* [8] proposed the Manhattan world assumption for human navigation. The origin of the world coordinates can be defined using the cubes and planes found in scenes because the assumption is that indoor and city scenes include many orthogonal lines. In particular, most images of buildings satisfy this assumption. A Manhattan world is useful for creating geometric constraints in robust simultaneous localization and mapping methods [11, 52]. In addition, a room-layout estimation method using panorama images and a Manhattan world was proposed by Jia *et al.* [10]. In these methods, the Manhattan world has pan-angle ambiguity; that is, the definition of two axes on the ground is arbitrary.

**Camera calibration.** To match 3D world coordinates and 2D image coordinates, camera calibration estimates the extrinsic and intrinsic camera parameters in a camera model. The extrinsics express the camera rotation in terms of pan, tilt, and roll angles, and the intrinsics represent the focal length, lens distortion, and image sensor specifications. Perspective camera calibration methods in the Manhattan world have been proposed for geometry-based methods [18, 28, 39, 42], combined geometry-based and learning-based methods [14, 16, 17, 43, 50, 58], and a learning-based method [22]. However, these methods address only narrow FOV cameras without distortion.

In this paper, we focus on calibration methods that both recover rotation and remove distortion from a single image in Table 1. A pioneering learning-based method was proposed by López-Antequera *et al.* [26] to address rotation and distortion. Wakai *et al.* [45, 46] proposed learning-based methods for fisheye cameras. However, these methods cannot predict pan angles.

Wildenauer *et al.* [49] proposed a pioneering geometry-based calibration method in a Manhattan world from a single image. This method addressed distortion using a one-parameter division model [9]. On the basis of Wildenauer's method, calibration methods have been proposed to improve calibration accuracy [2, 25, 35]. Although these

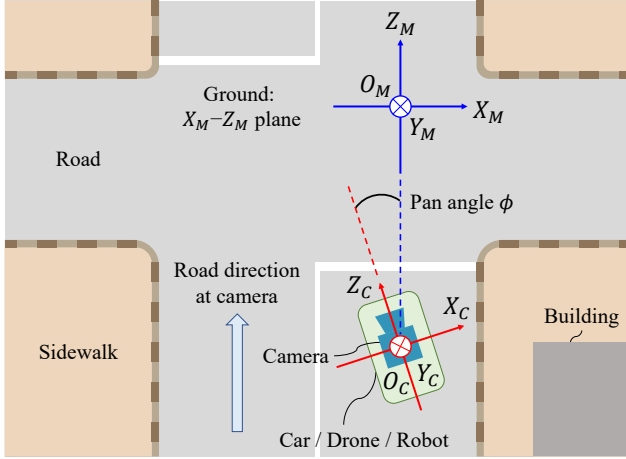


**Figure 2:** Definition of world coordinates in our Manhattan world. The origins of the world coordinates of our Manhattan world and camera are  $O_M$ - $X_M Y_M Z_M$  and  $O_C$ - $X_C Y_C Z_C$ , respectively. Each wall of cuboid buildings is parallel to the corresponding planes in  $O_M$ - $X_M Y_M Z_M$ . The cyan arrow indicates the direction of the road from the point of view of a camera mounted on a car, drone, or robot.

geometry-based methods can estimate pan angles, three aspects require improvement: 1) the pan angles have four-fold rotational symmetric ambiguity; 2) images with few arcs degrade the performance because of a lack of constraints; and 3) camera models do not support FOVs of over  $180^\circ$ .

### 3. Proposed method

First, we describe our proposed definition of pan angles in a Manhattan world to eliminate ambiguity. Second, we describe our learning-based calibration method using heatmap regression to recover fisheye images. Third, we introduce ADPs. Finally, we present the calibration pipeline.

#### 3.1. Proposed Manhattan world

**Definition of a pan angle.** The Manhattan world assumption [8] regards the world as consisting of grid-shaped roads; that is, two of the three orthogonal coordinate axes lie along a crossroads, and the remaining axis is vertical in Figure 2. We must define the origin of the pan angle from the four directions at a crossroads. Conventional methods [2, 25, 35, 49] randomly select the origin of the pan angles in the Manhattan world; that is, the range of a pan angle is from  $-45^\circ$  to  $45^\circ$  with four-fold rotational symmetric ambiguity. To address this pan-angle ambiguity, we propose the following alternative definition of pan angles in the Manhattan world. We select the axis  $\vec{Z}_M$  (a unit vector for the  $Z_M$  axis) in the Manhattan world along the direction of a road with respect to a camera in Figure 2. Note that in practice, we select the  $\vec{Z}_M$  satisfying the smallest

angle formed by  $\vec{Z}_M$  and  $\vec{Z}_C$  to remove two-fold rotational ( $180^\circ$ ) symmetric ambiguity because cameras are generally oriented to obtain the front view of cars, drones, or robots. Therefore, the pan angles in our method range from  $-90^\circ$  to  $90^\circ$  with respect to the direction of a road from the camera’s location. In contrast to previous methods, our pan-angle definition does not lead to ambiguities.

**Direction alignment.** For our Manhattan world, we need to select the origin of the pan angles that satisfies the smallest angle formed by  $\vec{Z}_M$  and  $\vec{Z}_C$  described in the pan-angle definition. In other words, we cannot distinguish a travel direction from a non-travel direction on a straight road. To make this selection, we align the direction to obtain the appropriate origin. Therefore, when we encounter a travel-direction ambiguity, we align direction labels using  $180^\circ$  rotation along the  $Y_M$  axis to remove this ambiguity. We  $180^\circ$ -rotationally align all labels based on two conditions: 1) the images have back labels without front labels; and 2) the images have right labels without front and left labels. These label details are explained in Section 3.3.

#### 3.2. Proposed calibration method

**Camera model.** Camera models express a mapping from world coordinates  $\tilde{\mathbf{p}}$  to image coordinates  $\tilde{\mathbf{u}}$  in homogeneous coordinates. This mapping is conducted using extrinsic and intrinsic parameters. Extrinsic parameters  $[\mathbf{R} \mid \mathbf{t}]$  consist of a rotation matrix  $\mathbf{R}$  and a translation vector  $\mathbf{t}$  to represent the relation between the origins of the camera coordinates and Manhattan world coordinates. The intrinsic parameters are focal length  $f$ , distortion  $\gamma$ , image sensor pitch  $(d_u, d_v)$ , and a principal point  $(c_u, c_v)$ . The subscripts  $u$  and  $v$  indicate the horizontal and vertical directions, respectively. The mapping is formulated as

$$\tilde{\mathbf{u}} = \begin{bmatrix} \gamma/d_u & 0 & c_u \\ 0 & \gamma/d_v & c_v \\ 0 & 0 & 1 \end{bmatrix} [\mathbf{R} \mid \mathbf{t}] \tilde{\mathbf{p}}. \quad (1)$$

To handle an FOV that is over  $180^\circ$ , we use the state-of-the-art generic camera model [45] to express the distortion, which is given by

$$\gamma = f \cdot (\eta + k_1 \eta^3), \quad (2)$$

where  $\eta$  is the incident angle and  $k_1$  is the distortion coefficient.

**Network architecture.** For the pan angles in our proposed Manhattan world, we need to recognize the road direction with respect to the camera in Figure 2. To address this problem, we distinguish four VP directions:  $\vec{X}_M$ ,  $-\vec{X}_M$ ,  $\vec{Z}_M$ , and  $-\vec{Z}_M$ . By contrast, conventional methods [4, 7, 13, 37, 38, 53] cannot distinguish these directions. Considering the four directions, we propose a deep neural network, called the "VP estimator," that detects these directions as labeled image coordinates, similar to keypoints.

This task corresponds to the detection of keypoints in geometric relationships, such as single human pose estimation [1]. Additionally, Wakai *et al.* [45] reported that mismatches in dataset domains degrade calibration accuracy. This degradation suggests that regressors consisting of fully connected layers extract domain-specific features without geometric cues such as VPs. In contrast to conventional regressors, heatmap regressors using 2D Gaussian kernels on labeled points have the potential for pixel-wise accuracy in pose estimation [30]. Therefore, we use heatmap regression for VPs, which is likely to avoid such degradation.

To estimate camera rotation, we require intrinsic parameters that project image coordinates to 3D incident ray vectors because the rotation is calculated using these incident ray vectors in our Manhattan world coordinates. For the intrinsics, we use Wakai’s calibration network [45] without the tilt and roll angle regressors, which is called the "distortion estimator." Therefore, our network has two branches in Figure 1. Notably, our network only requires a single image and does not need geometry-based arc detectors.

**Implementation details.** We use the HRNet [41] backbone, which has shown strong performance in various tasks, for our VP estimator. We found that the HRNet loss function evaluates only images that include detected keypoints; that is, detection failure does not affect the loss value. To tackle this problem, we modified this loss function to evaluate all images, including those with detection failure. This modification is suitable for deep single image camera calibration because, unlike human pose estimation, we always estimate camera rotation. To achieve sub-pixel precision, DARK [54] is applied to the heatmaps as postprocessing. Note that we do not employ DARK to generate heatmaps as a preprocessing step because such preprocessing leads to inconsistency between the heatmaps and camera parameters. Rectangular images are center cropped for the VP estimator.

### 3.3. Auxiliary diagonal points

For estimating camera rotation, VPs are strong geometric cues. Images often have one or no VPs, although unique rotation requires at least two unique axes that consist of lines through 3D VPs and the origin of the world coordinates. To solve this problem, we define additional VP-related points called ADPs. We found that six 3D VPs form a regular octahedron that has the symmetry of regular octahedron groups (octahedral symmetry) in Figure 3. This symmetry means that a regular octahedron has three types of rotational symmetric axes. To estimate a unique rotation, the point arrangement prefers 3D spatial uniformity, such as regular polygons. Considering the spatial uniformity and number of points, we use ADPs, which are the eight diagonal points that indicate the directions of the cubic corners in Table 2. This arrangement of VPs and ADPs (VP/ADPs) also has the symmetry of regular octahedron

**Table 2:** Labels of vanishing points and auxiliary diagonal points

Label name	Direction	Image coordinate <sup>1</sup>
Vanishing point		
front	$\vec{Z}_M$	$(W/2, H/2)$
back	$-\vec{Z}_M$	$(0, H/2)$
left	$-\vec{X}_M$	$(W/4, H/2)$
right	$\vec{X}_M$	$(3W/4, H/2)$
top	$-\vec{Y}_M$	$(0, 0)$
bottom	$\vec{Y}_M$	$(0, H)$
Auxiliary diagonal point		
front-left-top (FLT)	$(\vec{Z}_M - \vec{X}_M - \vec{Y}_M)/\sqrt{3}$	$(3W/8, H/4)$
front-right-top (FRT)	$(\vec{Z}_M + \vec{X}_M - \vec{Y}_M)/\sqrt{3}$	$(5W/8, H/4)$
front-left-bottom (FLB)	$(\vec{Z}_M - \vec{X}_M + \vec{Y}_M)/\sqrt{3}$	$(3W/8, 3H/4)$
front-right-bottom (FRB)	$(\vec{Z}_M + \vec{X}_M + \vec{Y}_M)/\sqrt{3}$	$(5W/8, 3H/4)$
back-left-top (BLT)	$(-\vec{Z}_M - \vec{X}_M - \vec{Y}_M)/\sqrt{3}$	$(W/8, H/4)$
back-right-top (BRT)	$(-\vec{Z}_M + \vec{X}_M - \vec{Y}_M)/\sqrt{3}$	$(7W/8, H/4)$
back-left-bottom (BLB)	$(-\vec{Z}_M - \vec{X}_M + \vec{Y}_M)/\sqrt{3}$	$(W/8, 3H/4)$
back-right-bottom (BRB)	$(-\vec{Z}_M + \vec{X}_M + \vec{Y}_M)/\sqrt{3}$	$(7W/8, 3H/4)$

<sup>1</sup> The  $W$  and  $H$  denote panorama image width and height, respectively.

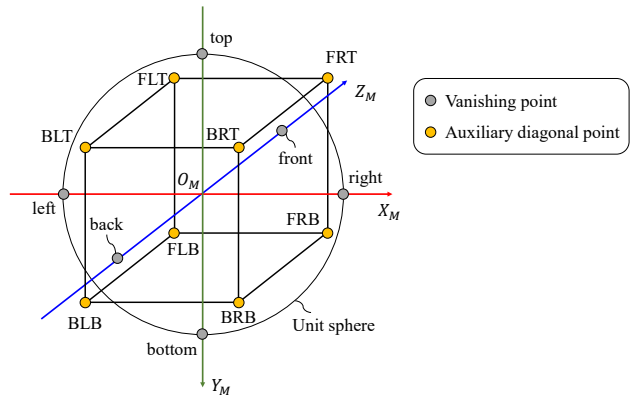


**Figure 3:** Coordinates of VPs and ADPs in our Manhattan world. The labels of the VPs and ADPs correspond to the labels described in Table 2.

groups and the greatest spatial uniformity in the case of eight points because of the diagonal directions, as shown in Figure 3. Therefore, 3D VP/ADP coordinates are the optimal arrangement. Details of the symmetry can be found in the appendix.

### 3.4. Calibration pipeline

**Overview.** Figure 4 shows our calibration pipeline for the inference. First, we obtain the VP/ADPs from the VP estimator and intrinsics from the distortion estimator. Second, these 2D VP/ADPs are projected onto a unit sphere in world coordinates using backprojection. Finally, we convert 3D VP/ADPs to the extrinsics as follows.

**Rotation estimation.** Here, we describe the estimation of camera rotation from the VP/ADPs. The estimation principle is to fit two sets of world coordinates and is known as the absolute orientation problem [48]. One set of world coordinates consists of the 3D VP/ADPs projected by back-

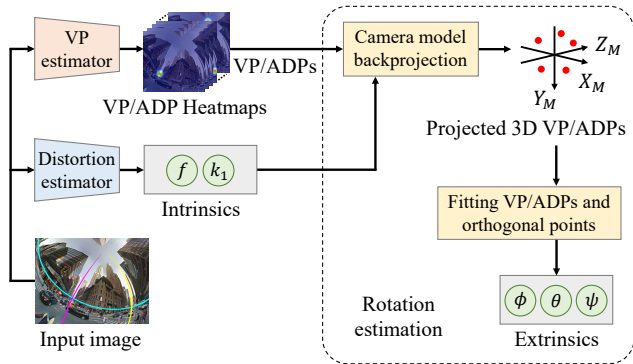


**Figure 4:** Calibration pipeline in the inference. The intrinsics are predicted by the distortion estimator. Camera models project VP/ADPs on the unit sphere by backprojection. The extrinsics are calculated from the fitting. The input image is generated from [32].

**Table 3:** Number of panoramas and fisheye image patches

Dataset	Panorama		Fisheye	
	Train	Test	Train	Test
SL-MH	55,599	161	555,990	16,100
SL-PB	57,840	167	578,400	16,700
SP360	19,038	55	571,140	16,500
HoliCity	6,235	18	561,150	16,200

projection [45] using the camera parameters. The other set consists of the 3D points corresponding to these VP/ADPs along the orthogonal Manhattan world coordinates shown in Figure 3. In our case, we focus on rotation without translation and scaling because all 3D points are on a unit sphere. In this fitting, we use the optimal linear attitude estimator [27, 33] that calculates the Rodrigues vector expressing the principal axis and angle. This Rodrigues vector is compatible with a quaternion, and we can obtain pan, tilt, and roll angles from this quaternion. Note that we regard undeterminable angles as  $0^\circ$  when point detection fails or an image has one or no axes from the VP/ADPs. The appendix presents details of the rotation estimation.

## 4. Experiments

To demonstrate validity and effectiveness of our approach, we employed extensive experiments using large-scale synthetic datasets and off-the-shelf fisheye cameras.

### 4.1. Datasets

We used three large-scale datasets of outdoor panoramas, the StreetLearn dataset [32], the SP360 dataset [5], and the HoliCity dataset [57]. In StreetLearn, we used the Manhattan 2019 subset (SL-MH) and the Pittsburgh 2019 subset (SL-PB). Following [45], we generated fisheye images using generic camera models with the ground-truth (GT) camera parameters in Table 3, and we captured outdoor images in Kyoto, Japan, using six off-the-shelf fisheye cameras.

**Table 4:** Distribution of the number of unique axes (%)

Dataset <sup>1</sup>	Number of unique axes							
	0	1	2	3	4	5	6	7
Train	0.0	1.3	13.5	25.7	24.8	18.8	10.9	5.1
Test	0.0	1.4	12.8	25.7	25.6	19.6	10.2	4.6

<sup>1</sup> SL-MH, SL-PB, SP360, and HoliCity all have the same distribution of the number of unique axes shown in this table

### 4.2. Parameter and label settings

**Parameter settings.** Following [45], we fixed the image sensor height to 24 mm,  $d_u = d_v$ , used the principal points  $(c_u, c_v)$  as the image center, and the translation vectors  $t$  as the zero vectors. Therefore, in our method, we focused on the estimation of five camera parameters, that is, focal length  $f$ , distortion coefficient  $k_1$ , pan angle  $\phi$ , tilt angle  $\theta$ , and roll angle  $\psi$  in our Manhattan world. We independently trained the VP estimator and distortion estimator using a mini-batch size of 32. We optimized the VP estimator, which was pretrained on ImageNet [36], using the Adam optimizer [12] and Random Erasing augmentation [56] with  $(p, s_l, s_h, r_1, r_2) = (0.5, 0.02, 0.33, 0.3, 3.3)$ . The initial learning rate was set to  $1 \times 10^{-4}$  and was multiplied by 0.1 at the 100th epoch. We also trained the distortion estimator pretrained on Wakai’s original network [45] using the RAdam optimizer [23] with a learning rate of  $1 \times 10^{-5}$ .

**Label settings.** We ignored *back* labels because the training and test sets had only 0.1% and 0.3% back labels, respectively, after direction alignment. Therefore, the VP estimator predicted 13 points, that is, the five VPs and eight ADPs in Table 2, without ambiguity. If all points are detected, our method can estimate a unique rotation for over 98% images with two or more unique axes from the VP/ADPs, as shown in Table 4.

### 4.3. Experimental results

We implemented comparison methods according to the corresponding papers but trained them on SL-MH, SL-PB, SP360, and HoliCity.

#### 4.3.1 Vanishing point estimation

To demonstrate the validity and effectiveness of the proposed VP estimator, we used pose estimation metrics and the distance error between the predicted and ground-truth VP/ADPs. Following [3], we used the standard keypoint metrics of the average precision (AP) and average recall (AR) [41] with a 5.6-pixel  $sk_i$  object keypoint similarity [29] as well as the percentage of correct keypoints (PCK) [1] with a 5.6-pixel distance threshold, which corresponds to 1/10th of the heatmap height.

Overall, the VP estimator detected the VP/ADPs, although the performance in the cross-domain evaluation decreased in Table 5. The AP, AR, and PCK results suggest

**Table 5:** Results of the cross-domain evaluation for our VP estimator using HRNet-W32

Dataset		Keypoint metric $\uparrow$							Mean distance error [pixel] $\downarrow$							
Train	Test	AP	AP <sup>50</sup>	AP <sup>75</sup>	AR	AR <sup>50</sup>	AR <sup>75</sup>	PCK	front	left	right	top	bottom	VP <sup>1</sup>	ADP <sup>1</sup>	All <sup>1</sup>
SL-MH	SL-MH	0.99	0.99	0.99	0.97	0.98	0.98	0.99	2.67	2.90	2.52	1.90	1.72	2.39	3.64	3.10
	SL-PB	0.98	0.99	0.99	0.96	0.97	0.97	0.98	3.51	3.50	3.11	2.34	2.02	2.97	4.52	3.85
	SP360	0.85	0.94	0.90	0.79	0.87	0.83	0.83	6.55	7.42	6.18	5.34	11.77	7.44	14.95	11.57
	HoliCity	0.80	0.92	0.86	0.72	0.83	0.78	0.77	9.73	12.27	9.75	8.54	6.60	9.47	17.92	14.11
SL-PB	SL-MH	0.99	0.99	0.99	0.96	0.97	0.97	0.99	3.26	3.49	3.10	2.04	1.74	2.79	4.63	3.84
	SL-PB	0.99	0.99	0.99	0.97	0.97	0.97	0.99	2.91	2.93	2.48	1.97	1.80	2.49	3.68	3.17
	SP360	0.82	0.92	0.87	0.75	0.85	0.81	0.81	7.72	8.65	7.53	5.41	12.74	8.42	15.88	12.53
	HoliCity	0.77	0.91	0.83	0.70	0.82	0.76	0.74	11.33	13.33	11.34	10.63	7.14	10.84	19.49	15.60
SP360	SL-MH	0.95	0.98	0.97	0.89	0.91	0.91	0.94	5.13	5.38	4.46	4.24	4.67	4.88	9.78	7.63
	SL-PB	0.95	0.98	0.97	0.88	0.91	0.90	0.94	4.66	4.86	4.12	4.83	3.69	4.50	10.14	7.66
	SP360	0.99	1.00	1.00	0.98	0.98	0.98	0.99	2.64	2.61	2.37	1.78	1.80	2.29	3.20	2.81
	HoliCity	0.79	0.92	0.85	0.69	0.79	0.75	0.77	12.44	14.20	11.33	8.20	6.02	10.70	19.38	15.45
HoliCity	SL-MH	0.95	0.98	0.97	0.89	0.91	0.91	0.95	4.80	5.07	4.44	3.89	4.50	4.61	10.50	7.69
	SL-PB	0.95	0.98	0.97	0.89	0.91	0.91	0.95	5.11	5.00	4.22	4.67	3.65	4.64	10.23	7.76
	SP360	0.89	0.96	0.93	0.84	0.90	0.87	0.88	5.42	6.75	6.05	3.34	9.59	6.20	12.11	9.48
	HoliCity	0.98	0.99	0.99	0.95	0.96	0.96	0.98	3.44	3.87	3.30	3.30	2.66	3.36	5.70	4.68

<sup>1</sup> "VP" denotes all 5 VPs; "ADP" denotes all 8 ADPs; "All" denotes all points consisting of 5 VPs and 8 ADPs

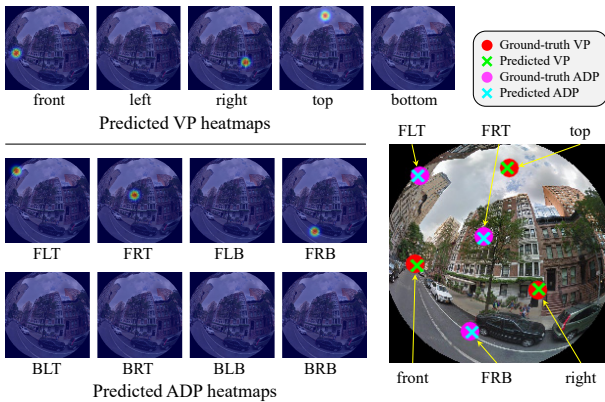


**Figure 5:** Qualitative results of VP/ADP detection using the proposed VP estimator on the test set of SL-MH. The VP estimator predicts five VP and eight ADP heatmaps for each VP/ADP.

that VP/ADP estimation is an easier task than human pose estimation because the VP/ADPs have the implicit constraints of the geometric coordinates shown in Figure 3. Table 5 also reveals that ADP detection is more difficult than VP detection because VPs generally have specific appearances at infinity. In the cross-domain evaluation, models trained by HoliCity could adapt well to other domains. In terms of distance errors, the VP estimator addressed the various directions of VP/ADPs. In addition, considering the qualitative results in Figure 5, the VP estimator stably detected VP/ADPs in the entire image. Therefore, the VP estimator can precisely detect VP/ADPs from a fisheye image.

### 4.3.2 Parameter and reprojection errors

To validate the accuracy of the camera parameters, we compared our method with conventional methods that estimate both rotation and distortion. Following [45], we evaluated

the mean absolute error and reprojection error (REPE). Our method achieved the lowest mean absolute angle error and REPE of the methods listed in Table 6. In our Manhattan world without pan-angle ambiguity, our method predicts wider pan-angle ranges than conventional methods. The pan-angle errors in our method using HRNet-W32 for the VP estimator are substantially smaller than those of Lochman’s method [25] by 20.16° on the test set of SL-MH. Our method also achieved 3.15° and 3.00° errors for the tilt and roll angles, respectively, outperforming the other methods. We evaluated our method using HRNet-W48 (a larger backbone) and obtained a slight RMSE improvement of 0.16 pixels with respect to the RMSE obtained using HRNet-W32.

Pritts’s [35] and Lochman’s [25] methods could not perform calibration for some images because of a lack of arcs. In particular, Lochman’s method [25] had 59.1% of the executable rate, that is, the number of successful executions divided by the number of all images. By contrast, our learning-based method can address arbitrary images independent of the number of arcs; that is, it demonstrates scene robustness. Compared with methods [25, 35] estimating the pan angles, our method using HRNet-W32 achieved a mean frames per second (fps) that was at least 280 times higher. Note that our test platform was equipped with an Intel Core i7-6850K CPU and an NVIDIA Geforce RTX 3080Ti.

We validated the effectiveness of the ADPs. Table 6 suggests that our method based on HRNet-W32 and VP/ADPs notably improved angle estimation compared with our method without the ADPs by 15.4° on average for pan, tilt, and roll angles. Therefore, ADPs dramatically alleviate the problems caused by a lack of VPs.

Additionally, we tested our proposed method using various datasets to validate its robustness. Table 7 shows that our method outperforms both existing state-of-the-art

**Table 6:** Comparison of the absolute parameter errors and reprojection errors on the test set of SL-MH

Method	Backbone	Mean absolute error <sup>1</sup> ↓						REPE <sup>1</sup> ↓	Executable rate <sup>1</sup> ↑	Mean fps <sup>2</sup> ↑	#Params	GFLOPs	
		Pan $\phi$		Tilt $\theta$	Roll $\psi$	$f$	$k_1$						
		[-45, 45]	[-90, 90] <sup>3</sup>										
López-A. [26]	CVPR'19	DenseNet-161	-	-	27.60	44.90	2.32	-	81.99	100.0	36.4	27.4M	7.2
Wakai [46]	ICCVW'21	DenseNet-161	-	-	10.70	14.97	2.73	-	30.02	100.0	33.0	26.9M	7.2
Wakai [45]	ECCV'22	DenseNet-161	-	-	4.13	5.21	0.34	0.021	7.39	100.0	25.4	27.4M	7.2
Pritts [35]	CVPR'18	-	25.35	-	42.52	18.54	-	-	-	96.7	0.044	-	-
Lochman [25]	WACV'21	-	22.36	-	44.42	33.20	6.09	-	-	59.1	0.016	-	-
Ours w/o ADPs	( 5 points) <sup>4</sup>	HRNet-W32 <sup>4</sup>	-	19.38	13.54	21.65	0.34	0.020	28.90	100.0	12.7	53.5M	14.5 <sup>4</sup>
Ours w/o VPs	( 8 points)	HRNet-W32	-	10.54	11.01	8.11	0.34	0.020	19.70	100.0	12.6	53.5M	14.5
Ours	(13 points)	HRNet-W32	-	<b>2.20</b>	<b>3.15</b>	<b>3.00</b>	0.34	0.020	<b>5.50</b>	100.0	12.3	53.5M	14.5
Ours	(13 points)	HRNet-W48	-	<b>2.19</b>	<b>3.10</b>	<b>2.88</b>	0.34	0.020	<b>5.34</b>	100.0	12.2	86.9M	22.1

<sup>1</sup> Units: pan  $\phi$ , tilt  $\theta$ , and roll  $\psi$  [deg];  $f$  [mm];  $k_1$  [dimensionless]; REPE [pixel]; Executable rate [%]

<sup>2</sup> Implementations: López-A. [26], Wakai [46], Wakai [45], and ours using PyTorch [34]; Pritts [35] and Lochman [25] using MATLAB

<sup>3</sup> Our Manhattan world has ranges from  $-90^\circ$  to  $90^\circ$  for pan angles

<sup>4</sup> (· points) is the number of VP/ADPs for VP estimators; VP estimator backbones are indicated; Rotation estimation in Figure 4 is not included in GFLOPs

**Table 7:** Comparison of the mean absolute rotation errors in degrees on the test sets of each dataset

Dataset	Wakai [45]			Lochman [25]			Ours (HRNet-W32)		
	Pan	Tilt	Roll	Pan	Tilt	Roll	Pan	Tilt	Roll
SL-MH	-	4.13	5.21	22.36	44.42	33.20	<b>2.20</b>	<b>3.15</b>	<b>3.00</b>
SL-PB	-	4.06	5.71	23.45	44.99	30.68	<b>2.30</b>	<b>3.13</b>	<b>3.09</b>
SP360	-	3.75	5.19	22.84	45.38	31.91	<b>2.16</b>	<b>2.92</b>	<b>2.79</b>
HoliCity	-	6.55	16.05	22.63	45.11	32.58	<b>3.48</b>	<b>4.08</b>	<b>3.84</b>

**Table 8:** Comparison on the cross-domain evaluation of the mean absolute rotation errors in degrees

Dataset	Wakai [45]			Ours (HRNet-W32)				
	Train	Test	Pan	Tilt	Roll	Pan	Tilt	Roll
SL-MH	SL-PB	-	5.51	12.02	2.98	<b>3.72</b>	<b>3.63</b>	
	SP360	-	9.11	37.54	8.06	<b>8.34</b>	<b>7.77</b>	
	HoliCity	-	10.94	42.20	10.74	<b>10.60</b>	<b>8.93</b>	

learning-based [45] and geometry-based [25] methods on all datasets in terms of rotation errors. Table 8 also reports that our method is superior to Wakai’s method [45], which tended to estimate the roll angle poorly in the cross-domain evaluation, especially on the HoliCity test set. We found that Wakai’s method [45] often recovered images upside down in a cloudy sky. This observation suggests that regression-based methods that do not use heatmaps, such as Wakai’s method [45], tend to misinterpret the cloudy sky as a gray road. Note that the images in HoliCity were captured in London, where the weather is often cloudy all year round. This phenomenon implies that regression-based methods that do not use heatmaps predict the roll angles mainly based on the sky and road regions. Although the sky and roads generally occupy large areas of the image, these regions, which have fewer geometric cues, seem to lead to unstable prediction. By contrast, our method, which uses heatmaps, can extract robust features through geometric VP/ADPs. Therefore, our method achieved robust estimation in various domains.

### 4.3.3 Qualitative evaluation

To evaluate the recovered image quality, we performed calibration on synthetic images and off-the-shelf cameras.

**Synthetic images.** Figure 6 shows the qualitative results obtained on synthetic images. Our results are the most similar to the ground-truth images. By contrast, the quality of the recovered images that contained a few arcs was considerably degraded when the geometry-based methods proposed by Pritts [35] and Lochman [25] were used. Furthermore, the learning-based methods proposed by López-Antequera [26], Wakai [46], and Wakai [45] did not recover the pan angles. We note that our method can even calibrate images in which trees line a street.

**Off-the-shelf cameras.** Following [45], we also evaluated calibration methods using off-the-shelf cameras to validate the effectiveness of our method. Figure 7 shows the qualitative results using off-the-shelf fisheye cameras using SL-MH for training. Our method meaningfully outperformed Lochman’s method [25] in terms of recovered images. These results indicate robustness in our method for various types of camera projection.

## 5. Conclusion

**Limitations.** It is difficult to recover images when an input image includes one or no unique axes that can be identified from the VP/ADPs. We believe that subsequent studies extend this work to address this open challenge. Another promising direction for future work is to use several images or videos for input. We consider one image because our focus is to develop deep single image camera calibration.

We proposed a pan-angle definition for a Manhattan world to eliminate four-fold rotational symmetric ambiguity. For our Manhattan world, we proposed a learning-based method to address rotation and distortion from a single image. To recover the rotation, our heatmap-based VP estimator detects the VP/ADPs. Experiments demonstrated that our method remarkably outperforms conventional methods.

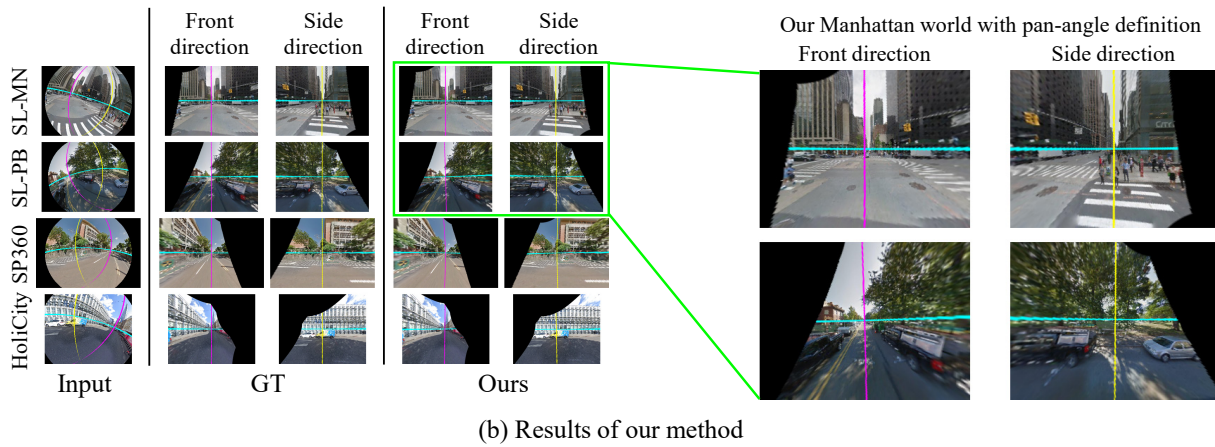
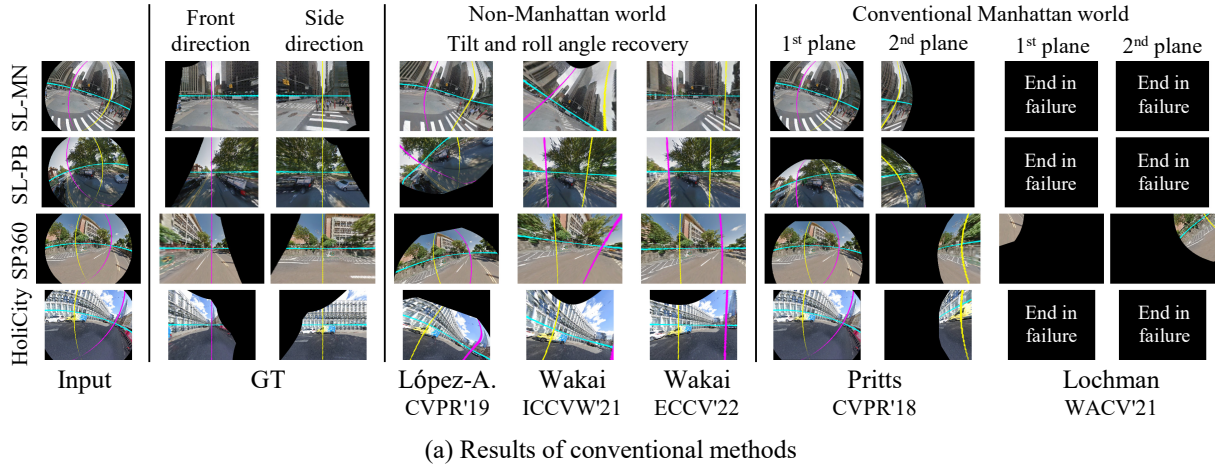


**Figure 6:** Qualitative results on the test sets. (a) Results of conventional methods. From left to right: input images, ground-truth images, and results of López-Antequera [26], Wakai [46], Wakai [45], Pritts [35], and Lochman [25]. (b) Results of our method. From left to right: input images, ground-truth images, and the results of our method using HRNet-W32 in our Manhattan world.

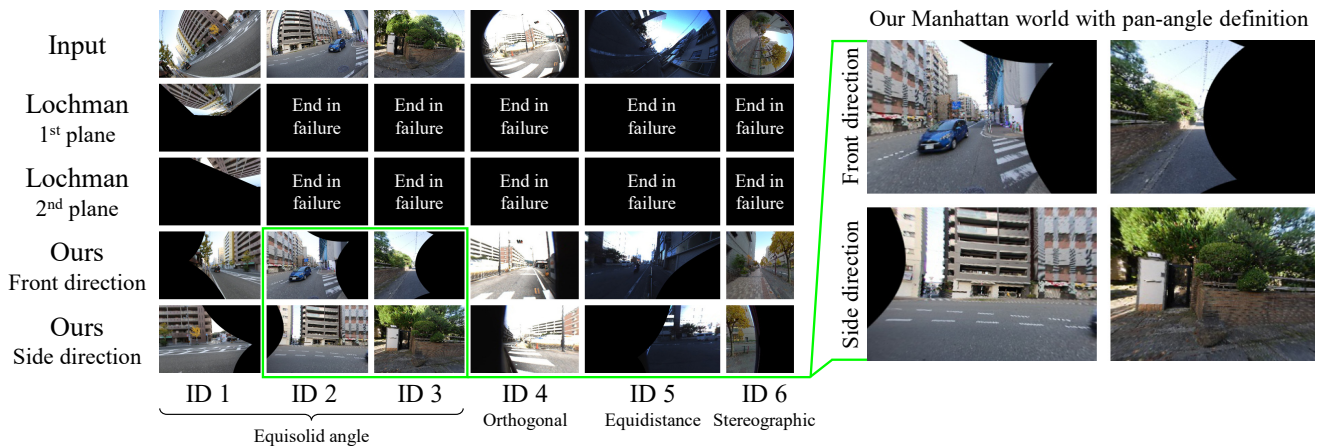


**Figure 7:** Qualitative results for images from off-the-shelf cameras. From top to bottom: input images, the results of the compared method (first and second planes obtained by Lochman [25]), and our method using HRNet-W32 (front and side direction images). The identifiers (IDs) correspond to the camera IDs used in [45], and the projection names are shown below the IDs.

## Appendix

**Structure of this appendix.** In this appendix, we present some omitted details: the novelty of our method in Section 6, details of our method of rotation estimation and auxiliary diagonal points in Section 7, and additional experimental results of the VP estimator and the whole of our method in Section 8.

### 6. Novelty

To describe the novelty of the paper, we again outline our major contributions:

1. We propose a definition of pan angles in a Manhattan world. The definition is based on the directions of roads with respect to the camera location and the travel direction, and it removes pan-angle ambiguity. To the best of our knowledge, we are the first researchers to calibrate pan angles without four-fold rotational symmetric ambiguity from a general scene image.
2. We propose a heatmap-based VP estimator for recovering the rotation from an image, to achieve higher accuracy and robustness than geometry-based methods using arc detectors.
3. We introduce auxiliary diagonal points with an optimal 3D arrangement based on the spatial uniformity of regular octahedron groups, to address the ambiguity caused by the lack of VPs in an image.

We explain the novelty of the paper, along with our contributions, in the remainder of this section.

**Our Manhattan world.** As the first contribution, image-based calibration in our proposed Manhattan world can estimate camera rotation as effectively as attitude estimation devices, such as odometry, gyros, and accelerator sensors. As explained in Section 1, to avoid obstacles, it is important to detect cars and pedestrians in front of a vehicle rather than at the sides in Figure 1. Our method is suitable for drones and smart glasses, whose space and weight are severely limited. This is because we can replace odometry, gyros, and accelerator sensors with the cameras that are generally attached to drones and smart glasses. For example, one of the types of sensing smart glasses in the Aria project [31] uses an inertial measurement unit for attitude estimation [24]. Therefore, our image-based method enables the downsizing of devices, such as drones and smart glasses, by replacing the devices that are currently used for attitude estimation.

**Heatmap-based vanishing point estimator.** As the second contribution, our heatmap-based VP estimator achieved the detection of VP/ADPs in general scene images. By contrast, conventional geometry-based methods [2, 25, 35, 49] use arc detectors for estimating VPs. However, detection

using arc detectors tends to fail in general scene images, such as images of trees lining a street. Furthermore, our VP estimator can robustly provide extrinsic camera parameters as VP/ADPs, in contrast to conventional learning-based methods [26, 45, 46] that use regressors without heatmaps. Our robust image-based method will contribute to subsequent studies; that is, robust camera rotation estimated by our method is useful for improving the performance of geometry-related tasks, such as simultaneous localization and mapping [11, 52].

**Auxiliary diagonal points.** As the third contribution, our proposed ADPs provide geometric cues that geometry-based methods cannot use; however, our heatmap-based VP estimator extracts these cues in general scene images. This approach of extracting geometric cues suggests that deep neural networks have the potential to obtain geometric cues that geometry-based methods cannot address. Similarly to our method, we believe that learning-based methods can use ADPs to improve their performance in geometry-related tasks, such as calibration, stereo matching, and simultaneous localization and mapping. In calibration, ADPs provide strong cues to alleviate the lack of VPs in images. Therefore, our method substantially outperformed both geometry-based [25, 35] and learning-based [26, 45, 46] state-of-the-art methods.

As described above, our major contributions have sufficient novelty to distinguish them from previous studies using both geometry-based and learning-based methods. Furthermore, we believe that our networks and ADPs will contribute to subsequent studies in many areas of computer vision, and are not limited to calibration.

### 7. Details of our method

In this section, we explain the details of our method of rotation estimation and describe the ADPs related to VPs.

#### 7.1. Rotation estimation

The details of rotation estimation are described in Section 3.4. As described there, the estimation is performed by fitting two sets of world coordinates, which is known as the absolute orientation problem [48]. One set of world coordinates  $U$  consists of the 3D VP/ADPs,  $\mathbf{p}$ , projected by back-projection [45] using the camera parameters on condition that the rotation matrix  $\mathbf{R}$  is a unit matrix and the translation vector  $\mathbf{t}$  is a zero-vector. The other set  $\hat{U}$  consists of the 3D points,  $\hat{\mathbf{p}}$ , that correspond to these VP/ADPs along our orthogonal Manhattan world coordinates, as shown in Figure 8. The absolute orientation problem is to fit the two sets,  $U$  and  $\hat{U}$ , by rotation, translation, and scaling. We focus only on rotation because VP/ADPs are in a unit sphere.

It should be noted that this problem cannot be solved in the case of two or fewer VP/ADPs. To handle this condition, we add additional points using the cross-product oper-

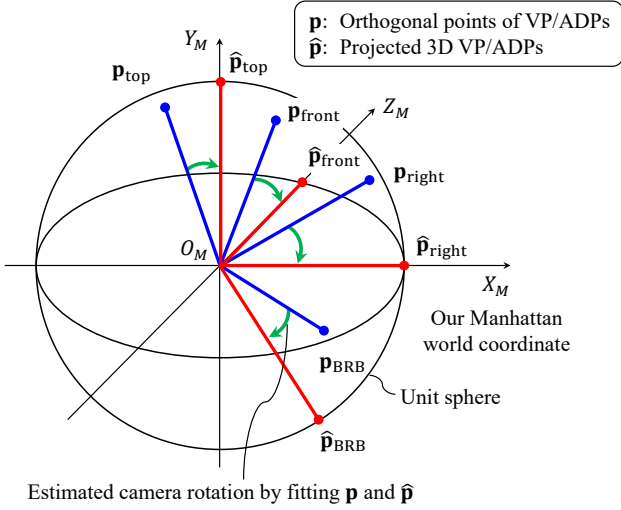


**Figure 8:** Projected 3D VP/ADPs and orthogonal points of VP/ADPs in our Manhattan world to estimate camera rotation. These orthogonal points are obtained as VP/ADPs without camera rotation; that is, pan, tilt, and roll angles are  $0^\circ$ . Four VP/ADPs of the labels in the front, right, top, and back-right-bottom (BRB) are shown in a unit sphere as an example of VP/ADPs.

ation. 1) In the case of two VP/ADPs, an additional point is calculated by the cross-product of the two position vectors of the VP/ADPs. 2) In the case of one VP/ADP, a temporal point on the unit sphere is added, whose direction is orthogonal to that of the VP/ADP. An additional point is calculated by the cross-product of the two position vectors of the temporal point and the VP/ADP. One of the angles (among the pan, tilt, and roll angles) of the temporal point is replaced by  $0^\circ$ . 3) In the case of no VP/ADPs,  $0^\circ$  is used for the pan, tilt, and roll angles.

Conventional methods to solve the absolute orientation problem are based on singular value decomposition. To reduce the computational costs, the optimal linear attitude estimator [27, 33] was proposed, which uses skew-symmetric matrices instead of singular value decomposition. We describe the procedure for obtaining the pan, tilt, and roll angles because conventional calibration methods report results with these angles rather than the Rodrigues vector. First, we estimate the camera rotation as the Rodrigues vector,  $\mathbf{g} = (g_x, g_y, g_z)^T$ , using this optimal linear attitude estimator. Second, we convert the Rodrigues vector  $\mathbf{g}$  to an optimal quaternion,  $\hat{q} = (\hat{q}_x, \hat{q}_y, \hat{q}_z, \hat{q}_w)$ , using the equation

$$\hat{q} = \frac{\mathbf{q}}{\sqrt{\mathbf{q}^T \mathbf{q}}}, \quad (3)$$

where  $\mathbf{q} = (g_x, g_y, g_z, 1)$  [33]. Third, we obtain a rotation

matrix  $\mathbf{R}$  from the quaternion  $\hat{q}$  using the equation

$$\mathbf{R} = \begin{bmatrix} a_w + a_x - 1 & a_{xy} - a_{zw} & a_{xz} + a_{yw} \\ a_{xy} + a_{zw} & a_w + a_y - 1 & a_{yz} - a_{wx} \\ a_{xz} - a_{yw} & a_{yz} + a_{wx} & a_w + a_z - 1 \end{bmatrix}, \quad (4)$$

where

$$\begin{aligned} (a_x, a_y, a_z, a_w) &= (2\hat{q}_x^2, 2\hat{q}_y^2, 2\hat{q}_z^2, 2\hat{q}_w^2), \\ (a_{xy}, a_{yz}, a_{zw}, a_{wx}) &= (2\hat{q}_x\hat{q}_y, 2\hat{q}_y\hat{q}_z, 2\hat{q}_z\hat{q}_w, 2\hat{q}_w\hat{q}_x), \\ (a_{xz}, a_{yw}) &= (2\hat{q}_x\hat{q}_z, 2\hat{q}_y\hat{q}_w). \end{aligned}$$

Finally, we calculate the pan, tilt, and roll angles by decomposing the rotation matrix. However, this decomposition is not unique without constraints. To solve this problem, we determined the pan, tilt, and roll angles for which the mean absolute angle errors between the predicted and ground-truth angles are the smallest, for both our method and conventional methods. It should be noted that, in our method, the predicted Rodrigues vector is directly used for applications, and the decomposition described above was employed to evaluate angle errors.

## 7.2. Symmetry of auxiliary diagonal points

We describe the optimal arrangement of ADPs in detail. Our calibration method requires at least two unique axes to estimate camera rotation without ambiguity. It is possible to add VP-related points, such as ADPs; however, increasing the number of points causes unstable optimization. To address this trade-off, we analyze the arrangement of VP/ADPs with respect to 3D spatial uniformity and the number of points.

In world coordinates at a unit sphere, VPs form a regular octahedron, shown in Figure 9(a). This regular octahedron has the symmetry of the regular octahedron groups, whose rotational symmetry has six axes in  $C_2$ , four axes in  $C_3$ , and three axes in  $C_4$ . It should be noted that  $C_n$  represents the rotational symmetry using Schoenflies notation; that is,  $C_n$  is  $(360^\circ/n)$ -rotational symmetry in Figure 9(b). We need to define VP-related points along  $C_2$ ,  $C_3$ , or  $C_4$  to maintain the symmetry of the regular octahedron groups; that is, these points are on the axes or form axial symmetry. Because of the trade-off described above, we focus on arrangements with a small number of points. Figure 9 shows arrangements of our proposed ADPs and candidate points, as explained below.

First, we explain the arrangement of ADPs illustrated in Figure 9(c). Along the  $C_3$  axes, ADPs are located at the eight corners of a cube. The minimum angle formed by two axes,  $\alpha$ , is  $54.7^\circ$ . This angle expresses the magnitude of the 3D spatial uniformity; that is, biased arrangements decrease  $\alpha$ . Second,  $C_3$ -based auxiliary points, of which there are 24, are defined along the  $C_3$  axes ( $C_3$ -axial symmetry), as shown in Figure 9(d). The number of points (24)

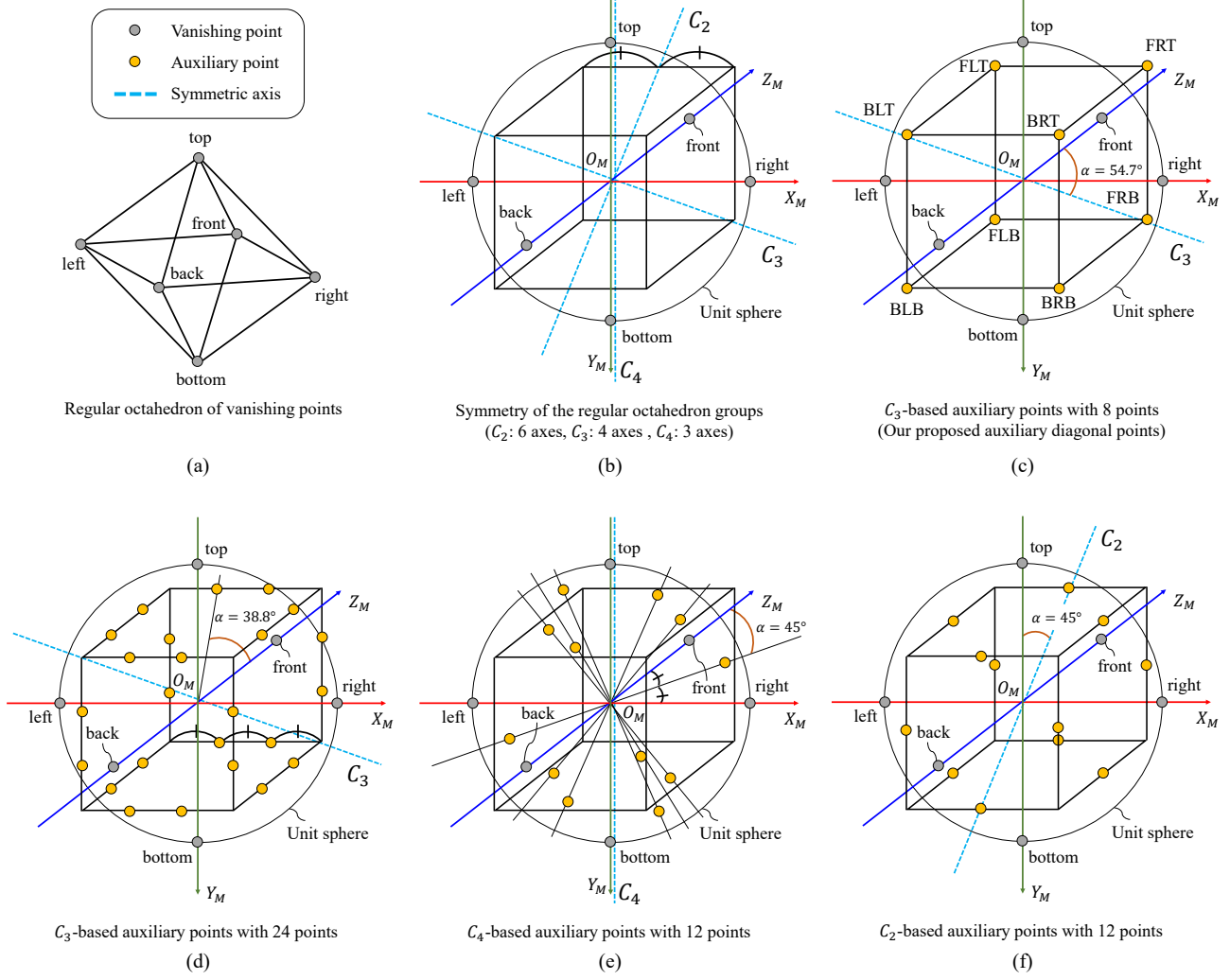


**Figure 9:** Arrangements of VPs and ADPs. (a) A regular octahedron formed by VPs. (b) Symmetry axes of  $C_2$ ,  $C_3$ , and  $C_4$  in the symmetry of the regular octahedron groups. (c) An arrangement of ADPs. (d) An arrangement of  $C_3$ -based auxiliary points with 24 points. (e) An arrangement of  $C_4$ -based auxiliary points with eight points. (f) An arrangement of  $C_2$ -based auxiliary points with 12 points.

**Table 9:** Comparison of the numbers of auxiliary points and minimum axis angles

Arrangement	Number of auxiliary points	Minimum axis angle $\alpha \uparrow$
$C_3$ -based auxiliary points in Figure 9(c) (ADPs)	8	$54.7^\circ$
$C_3$ -based auxiliary points in Figure 9(d)	24	$38.8^\circ$
$C_4$ -based auxiliary points in Figure 9(e)	12	$45.0^\circ$
$C_2$ -based auxiliary points in Figure 9(f)	12	$45.0^\circ$

is the second smallest number of points for the  $C_3$  axes because the  $C_3$  axes have  $120^\circ$ -rotational symmetry, yielding 24 points ( $8 \text{ axes} \times 360^\circ / 120^\circ$ -rotational symmetry). Third,  $C_4$ -based auxiliary points, of which there are 12, are defined along the  $C_4$  axes ( $C_4$ -axial symmetry), as shown in Figure 9(e). Each point is located on the bisector of an angle between two orthogonal axes: two axes among  $X_M$ ,  $Y_M$ , and  $Z_M$ . We use these axial-symmetric points because VPs

are located along the  $C_4$  axes. Fourth,  $C_2$ -based auxiliary points, of which there are 12, are defined along the  $C_2$  axes, as shown in Figure 9(f). Each point is located in the middle of the edge of a cube. It should be noted that we can assume other arrangements satisfying the symmetry of the regular octahedron groups, in addition to those above. These other arrangements have more auxiliary points than those in (c), (d), (e), and (f) have for each symmetric axis. Therefore, we

**Table 10:** Comparison of the distribution of the number of unique axes after direction alignment (%)

Dataset <sup>1</sup>	Number of unique axes							
	0	1	2	3	4	5	6	7
Only VPs (5 points)								
Train	0.9	48.4	31.5	19.2	-	-	-	-
Test	0.8	47.8	31.5	19.9	-	-	-	-
VPs and ADPs (13 points)								
Train	0.0	1.3	13.5	25.7	24.8	18.8	10.9	5.1
Test	0.0	1.4	12.8	25.7	25.6	19.6	10.2	4.6

<sup>1</sup> SL-MH, SL-PB, SP360, and HoliCity all have the same distribution of the number of unique axes, as shown in this table

focus on the arrangements illustrated in Figure 9 because many auxiliary points cause unstable optimization in training.

Of all the cases discussed above, the minimum number of points is eight, as shown in Figure 9(c). The number of ADPs (8) is smaller than that of  $C_2$ -based and  $C_4$ -based auxiliary points (12). In addition, ADPs have 3D spatial uniformity with respect to the minimum axis angle  $\alpha$ , as shown in Table 9. Therefore, we use ADPs, which have the optimal arrangement in the case of eight points, for our calibration method.

As described in Section 4.2, our method was able to estimate a unique rotation for over 98% of the images in our experiments because of the arrangement of optimal 3D spatial uniformity, as presented in Table 10. By contrast, the use of VPs without ADPs enabled the estimation of a unique rotation for less than 52% of the images. It should be noted that the number of unique axes was the same in the SL-MH, SL-PB, SP360, and HoliCity datasets because we used the same random distribution for generating fisheye images. Table 11 shows the number of VP/ADP labels in each dataset. The diagonal directions of ADPs led to increasing the number of ADPs in images. In particular, ADPs were arranged at the front side (FLT, FRT, FLB, and FRB) in over 35% of the images. Therefore, ADPs can alleviate the lack of VPs in images.

## 8. Experimental results

To demonstrate the validity and effectiveness of our method, we present further quantitative and qualitative results of our experiments in this section. The dataset names (SL-MH, SL-PB, SP360, and HoliCity) correspond to the names used in Section 4.1.

### 8.1. Results of training the distortion estimator

We report the performance of our distortion estimator to describe the difference between Wakai’s method [45] and the distortion estimator. Our distortion estimator is composed of Wakai’s calibration network [45] without the tilt

**Table 11:** Distribution of the number of labels after direction alignment (%)

Label name <sup>1</sup>	Train <sup>2</sup>	Test <sup>2</sup>
VPs		
front	57.2	46.9
back	0.1	0.3
left	37.6	42.3
right	21.3	19.2
top	26.6	31.0
bottom	26.5	31.3
ADPs		
FLT	50.6	47.8
FRT	41.9	35.5
FLB	50.5	47.9
FRB	41.7	35.2
BLT	16.0	21.6
BRT	7.2	9.2
BLB	15.9	22.0
BRB	7.2	9.1

<sup>1</sup> The labels of the VPs and ADPs correspond to the labels described in Table 2

<sup>2</sup> SL-MH, SL-PB, SP360, and HoliCity all have the same distribution of the number of unique axes, as shown in this table

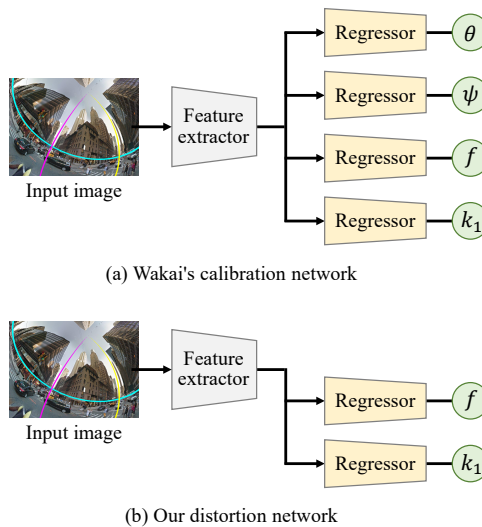


**Figure 10:** Network architectures of (a) Wakai’s calibration network [45] and (b) our distortion network. Wakai’s calibration network predicts extrinsics (tilt  $\theta$  and roll  $\psi$  angles) and intrinsics (focal length  $f$  and a distortion coefficient  $k_1$ ). By contrast, our distortion estimator has two regressors for the focal length  $f$  and distortion coefficient  $k_1$ . The input image is generated from [32].

and roll angle regressors, as shown in Figure 10. We optimized the distortion estimator after pretraining on Wakai’s calibration network. The distortion estimator achieved slight improvements in the focal length  $f$  and distortion coefficient  $k_1$  because the number of predicted camera parameters was reduced by two, that is, the tilt and roll angles, as shown in Table 12.

**Table 12:** Comparison of calibration accuracy by Wakai’s method [45] and our distortion estimator on the test sets of each dataset

Dataset	Wakai [45] ECCV’22					Our distortion estimator						
	Mean absolute error ↓				RSNR <sup>1</sup> ↑	SSIM <sup>1</sup> ↑	Mean absolute error ↓				RSNR ↑	SSIM ↑
	Tilt $\theta$ [deg]	Roll $\psi$ [deg]	$f$ [mm]	$k_1$			Tilt $\theta$ [deg]	Roll $\psi$ [deg]	$f$ [mm]	$k_1$		
SL-MH	4.13	5.21	0.34	0.021	29.01	0.838	–	–	0.34	<b>0.020</b>	<b>29.09</b>	<b>0.840</b>
SL-PB	4.06	5.71	0.36	0.024	29.05	0.826	–	–	0.36	<b>0.022</b>	<b>29.31</b>	<b>0.833</b>
SP360	3.75	5.19	0.39	0.023	28.10	0.835	–	–	<b>0.37</b>	0.023	<b>28.23</b>	<b>0.836</b>
HoliCity	6.55	16.05	0.48	0.028	25.59	0.751	–	–	0.48	0.028	<b>25.68</b>	<b>0.755</b>

<sup>1</sup> PSNR is the peak signal-to-noise ratio and SSIM is the structural similarity [47]

## 8.2. Comparison using ResNet backbones

To clarify the performance of the HRNet [41] backbones, we also evaluated our method using the ResNet [40] backbones, which are one of the baseline backbones used for various tasks. Table 13 shows the results of our method using either the ResNet or HRNet backbones. With respect to rotation errors and REPE [45], our method using the HRNet backbones outperformed that using the ResNet backbones, irrespective of backbone size. This benefit of the HRNet backbones corresponds to its advantages for human pose estimation [41]. Our method using HRNet-W48 achieved slight improvements over HRNet-W32 with respect to REPE and pan, tilt, and roll angles. The small magnitude of these improvements suggests that the performance is saturated for the larger HRNet-W48 backbone; this saturation may possibly be caused by the limitation of the variations of the panorama-image datasets.

## 8.3. Comparison using HRNet loss function

To validate the effectiveness of our loss function, we trained the VP estimator with HRNet-W32 using the HRNet loss function [41]. As described in Section 3.2, the HRNet loss function evaluates only images that include detected keypoints; that is, detection failure does not affect the loss value. To solve this problem, we modified this loss function to evaluate all images, including those with detection failure. Table 14 shows the results of our VP estimator trained using either the HRNet loss function or our loss function. In keypoint metrics, the VP estimator trained using our loss function improved AP, AR<sup>50</sup>, and AR<sup>75</sup> by 0.01 points, compared with the VP estimator trained using the HRNet loss function. The mean distance errors of all VP/ADPs in the VP estimator trained using our loss function are smaller than those in the VP estimator trained using the HRNet loss function by 0.08 pixels. In addition, the results in Table 15 show that our method trained using our loss function improved angle estimation by 0.17° on average, compared with our method using the HRNet loss function, for pan, tilt, and roll angles. Therefore, our loss function can improve the calibration accuracy of our method.

## 8.4. Error factor of our method

We analyzed the results of our method using HRNet-W32 to describe the error factor; that is, the calibration errors were caused by the distortion estimator and VP estimator. To evaluate this error factor, we performed calibration with ground-truth values for distortion parameters and image coordinates of VP/ADPs from the distortion estimator and the VP estimator, respectively, as shown in Table 16. Our method using ground-truth image coordinates of VP/ADPs outperformed our method using ground-truth distortion parameters, with respect to angle error and REPE. Therefore, the errors of the VP estimator were dominant over those of the distortion errors. In particular, angle errors were primarily caused by the VP estimator because camera rotation is mainly estimated from VP/ADPs. These results also show that the distortion estimator and VP estimator have room for improvement by  $-0.11^\circ$  and  $-1.58^\circ$ , respectively, on average for pan, tilt, and roll angles.

## 8.5. Details of quantitative results

To analyze the accuracy and robustness of our method, we evaluated our method and conventional methods on the test sets of SL-MH, SL-PB, SP360, and HoliCity. Table 17 shows the mean absolute errors and REPE [45]. It should be noted that we cannot calculate the REPE of Pritts’s [35] and Lochman’s [25] methods, for the following reasons: Pritts’s method does not predict focal length, which we need for calculating REPE; in Lochman’s method, the division camera model [9] cannot address projected sampling points with over 180° FOV because camera parameter errors lead to projected points with over 180° FOV. Table 18 also reports the results of the cross-domain evaluation. These results demonstrated that our method using HRNet-W32 outperformed methods proposed by López-Antequera [26], Wakai [46], Wakai [45], Pritts [35], and Lochman [25] in terms of the mean absolute errors and REPE.

## 8.6. Error distribution of our method

To evaluate the error distribution of angles, we compared the predicted and ground-truth camera parameters. Figure 11 shows the error distribution for our method using HRNet-W32. Although a few predicted angles have angle

**Table 13:** Comparison of ResNet and HRNet in our method on the test set of SL-MH

Backbone <sup>1</sup>	Mean absolute error <sup>2</sup> ↓			REPE <sup>2</sup> ↓	Mean fps <sup>3</sup> ↑	#Params	GFLOPs <sup>4</sup>
	Pan $\phi$	Tilt $\theta$	Roll $\psi$				
ResNet-50	4.89	4.97	4.79	8.39	<b>19.9</b>	58.7M	16.4
ResNet-101	3.65	4.07	3.87	7.02	17.7	76.8M	19.8
ResNet-152	3.46	3.80	3.72	6.68	16.0	91.8M	23.3
HRNet-W32	2.20	3.15	3.00	5.50	12.3	53.5M	14.5
HRNet-W48	<b>2.19</b>	<b>3.10</b>	<b>2.88</b>	<b>5.34</b>	12.2	86.9M	22.1

<sup>1</sup> Our VP estimator backbones are indicated

<sup>2</sup> Units: pan  $\phi$ , tilt  $\theta$ , and roll  $\psi$  [deg]; REPE [pixel]

<sup>3</sup> Implementations: our method using PyTorch [34]

<sup>4</sup> Rotation estimation in Figure 4 is not included

**Table 14:** Comparison of loss functions in our VP estimator using HRNet-W32 on the test set of SL-MH

Loss function	Keypoint metric ↑							Mean distance error [pixel] ↓							
	AP	AP <sup>50</sup>	AP <sup>75</sup>	AR	AR <sup>50</sup>	AR <sup>75</sup>	PCK	front	left	right	top	bottom	VP <sup>1</sup>	ADP <sup>1</sup>	All <sup>1</sup>
HRNet loss function [41]	0.98	0.99	0.99	0.97	0.97	0.97	0.99	<b>2.58</b>	<b>2.86</b>	2.55	1.90	<b>1.69</b>	<b>2.35</b>	3.80	3.18
Our loss function	<b>0.99</b>	0.99	0.99	0.97	<b>0.98</b>	<b>0.98</b>	0.99	2.67	2.90	<b>2.52</b>	1.90	1.72	2.39	<b>3.64</b>	<b>3.10</b>

<sup>1</sup> "VP" denotes all 5 VPs; "ADP" denotes all 8 ADPs; "All" denotes all points consisting of 5 VPs and 8 ADPs

errors, most predicted angles are plotted close to the diagonal lines in Figure 11. (Angles are plotted on the diagonal lines when the predicted angles correspond to the ground-truth angles.) This distribution indicates that our method can stably predict angles throughout the angle range from  $-90^\circ$  to  $90^\circ$ ; that is, it demonstrates angle robustness.

In addition, we analyzed the error distribution of camera parameters: angles, focal length, and distortion coefficients. We divided the angle range into 10 equal intervals:  $[-90^\circ, -72^\circ]$ ,  $[-72^\circ, -54^\circ]$ , ...,  $[72^\circ, 90^\circ]$ . Similarly, we divided the ranges of focal length and distortion coefficients into 10 equal intervals. The results for these subdivisions are shown using box and violin<sup>1</sup> plots in Figure 12. Each violin plot with a single peak indicates that our networks were sufficiently optimized because insufficient optimization leads to multiple peaks in violin plots. Overall, our method achieved precise calibration across the whole range of predicted angles.

## 8.7. Qualitative evaluation

To validate the VP/ADP estimation and quality of the recovered images, we present additional calibration results using synthetic images and off-the-shelf fisheye cameras.

### 8.7.1 Vanishing point estimation

To demonstrate the robustness of our heatmap-based VP estimator, we visualized the results of VP/ADPs. Figure 13 shows qualitative results of the VP estimator using HRNet-

<sup>1</sup>The violin plot represents the probability density of the distribution as the width of the violin plot, and supports multiple peaks. Two peaks of the probability density form the shape of a violin.

W32. Although the test images were affected by various types of rotation and distortion, the VP estimator achieved stable VP/ADP detection from the centers of images to their edges. Each predicted VP/ADP heatmap has a single peak for VP/ADPs. Such a single peak, with little noise, indicates that the VP estimator was well-optimized. In addition, many test images contain large regions of sky or road surface with few geometric cues such as arcs; however, the VP estimator handled these images successfully. Therefore, the VP estimator was able to robustly detect VP/ADPs.

### 8.7.2 Recovered images

**Synthetic images.** Figure 14 shows the additional qualitative results obtained on synthetic images. Similarly to Figure 6, our results are the most similar to the ground-truth images. By contrast, the quality of the recovered images that contain a few arcs was notably degraded when the geometry-based methods proposed by Pritts [35] and Lochman [25] were used. In particular, Lochman's method [25] tended to result in execution failure on these images. Additionally, the learning-based methods proposed by López-Antequera [26], Wakai [46], and Wakai [45] did not recover the pan angles; that is, vertical magenta and yellow lines are not located at the centers of the images produced by these methods, shown in Figure 14. We note that our method was able to calibrate images of streets lined by large trees.

To validate the effectiveness of our method, we also demonstrated the qualitative results in the cross-domain evaluation. Figure 15 shows the qualitative results in the cross-domain evaluation on the test set of HoliCity when

**Table 15:** Comparison of loss functions in our method using HRNet-W32 on the test set of SL-MH

Loss function	Mean absolute error <sup>1</sup> ↓			REPE <sup>1</sup> ↓
	Pan $\phi$	Tilt $\theta$	Roll $\psi$	
HRNet loss function [41]	2.54	3.25	3.07	5.60
Our loss function	<b>2.20</b>	<b>3.15</b>	<b>3.00</b>	<b>5.50</b>

<sup>1</sup> Units: pan  $\phi$ , tilt  $\theta$ , and roll  $\psi$  [deg]; REPE [pixel]

**Table 16:** Comparison using prediction and ground truth in our method using HRNet-W32 on the test set of SL-MH

Distortion parameter $f$ and $k_1$ (Distortion estimator)	Image coordinates of VP/ADPs (VP estimator)	Mean absolute error <sup>1</sup> ↓			REPE <sup>1</sup> (Gain) ↓
		Pan $\phi$ (Gain <sup>2</sup> )	Tilt $\theta$ (Gain)	Roll $\psi$ (Gain)	
Prediction	GT	<b>0.94</b> (-1.26)	<b>1.40</b> (-1.75)	<b>1.27</b> (-1.73)	<b>2.60</b> (-2.90)
GT	Prediction	2.21 (+0.01)	2.95 (-0.20)	2.86 (-0.14)	3.83 (-1.67)
Prediction	Prediction	2.20	3.15	3.00	5.50

<sup>1</sup> Units: pan  $\phi$ , tilt  $\theta$ , and roll  $\psi$  [deg]; REPE [pixel]

<sup>2</sup> The origin of the gain is that our method predicts both distortion parameters and image coordinates of VP/ADPs (bottom row)

learning-based methods were trained on SL-MH. Conventional learning-based methods tended to have rotation errors in the cross-domain evaluation, as shown in Table 18. As described in Section 4.3.2, conventional methods often recovered images upside down in a cloudy sky on input images with approximately  $\pm 90^\circ$ -roll angles. By contrast, our method, which uses heatmaps, can achieve robust estimation in various domains because of geometric VP/ADPs.

**Off-the-shelf cameras.** Following [45], we also evaluated calibration methods using six off-the-shelf fisheye cameras to validate the effectiveness of our method. Figure 16 shows the qualitative results on images from off-the-shelf fisheye cameras using SL-MH for training. Similarly to Figure 7, our method substantially outperformed the methods proposed by López-Antequera [26], Wakai [46], Wakai [45], Pritts [35], and Lochman [25] with respect to the quality of the recovered images. Furthermore, these results demonstrate the robustness of our method for four types of camera projection: equisolid angle projection, orthogonal projection, equidistant projection, and stereographic projection.

**Table 17:** Comparison of the absolute parameter errors and reprojection errors on the test sets of each dataset

Dataset	Method	Mean absolute error <sup>1</sup> ↓							REPE <sup>1</sup> ↓	Executable rate <sup>1</sup> ↑
		Pan $\phi$		Tilt $\theta$	Roll $\psi$	$f$	$k_1$			
		$[-45, 45]$	$[-90, 90]$ <sup>2</sup>							
SL-MH	López-A. [26]	CVPR'19	–	–	27.60	44.90	2.32	–	81.99	100.0
	Wakai [46]	ICCVW'21	–	–	10.70	14.97	2.73	–	30.02	100.0
	Wakai [45]	ECCV'22	–	–	4.13	5.21	0.34	0.021	7.39	100.0
	Pritts [35]	CVPR'18	25.35	–	42.52	18.54	–	–	–	96.7
	Lochman [25]	WACV'21	22.36	–	44.42	33.20	6.09	–	–	59.1
	Ours (HRNet-W32)		–	<b>2.20</b>	<b>3.15</b>	<b>3.00</b>	0.34	0.020	<b>5.50</b>	100.0
SL-PB	López-A. [26]	CVPR'19	–	–	26.18	41.94	2.11	–	73.68	100.0
	Wakai [46]	ICCVW'21	–	–	10.66	14.53	2.67	–	25.76	100.0
	Wakai [45]	ECCV'22	–	–	4.06	5.71	0.36	0.024	7.99	100.0
	Pritts [35]	CVPR'18	25.55	–	42.94	18.28	–	–	–	97.9
	Lochman [25]	WACV'21	23.45	–	44.99	30.68	8.14	–	–	39.1
	Ours (HRNet-W32)		–	<b>2.30</b>	<b>3.13</b>	<b>3.09</b>	0.36	0.022	<b>5.89</b>	100.0
SP360	López-A. [26]	CVPR'19	–	–	28.66	44.45	3.26	–	84.56	100.0
	Wakai [46]	ICCVW'21	–	–	11.12	17.70	2.67	–	32.01	100.0
	Wakai [45]	ECCV'22	–	–	3.75	5.19	0.39	0.023	7.39	100.0
	Pritts [35]	CVPR'18	25.39	–	42.79	18.35	–	–	–	98.5
	Lochman [25]	WACV'21	22.84	–	45.38	31.91	6.81	–	–	53.7
	Ours (HRNet-W32)		–	<b>2.16</b>	<b>2.92</b>	<b>2.79</b>	0.37	0.023	<b>5.60</b>	100.0
HoliCity	López-A. [26]	CVPR'19	–	–	65.92	50.31	2.27	–	96.63	100.0
	Wakai [46]	ICCVW'21	–	–	12.18	26.00	2.56	–	34.99	100.0
	Wakai [45]	ECCV'22	–	–	6.55	16.05	0.48	0.028	19.37	100.0
	Pritts [35]	CVPR'18	25.45	–	43.22	17.84	–	–	–	99.6
	Lochman [25]	WACV'21	22.63	–	45.11	32.58	6.71	–	–	83.9
	Ours (HRNet-W32)		–	<b>3.48</b>	<b>4.08</b>	<b>3.84</b>	0.48	0.028	<b>7.62</b>	100.0

<sup>1</sup> Units: pan  $\phi$ , tilt  $\theta$ , and roll  $\psi$  [deg];  $f$  [mm];  $k_1$  [dimensionless]; REPE [pixel]; Executable rate [%]<sup>2</sup> Our Manhattan world has ranges from  $-90^\circ$  to  $90^\circ$  for pan angles**Table 18:** Comparison on the cross-domain evaluation of the mean absolute rotation errors and reprojection errors

Dataset		López-A. [26] CVPR'19				Wakai [46] ICCVW'21				Wakai [45] ECCV'22				Ours (HRNet-W32)			
Train	Test	Pan <sup>1</sup>	Tilt <sup>1</sup>	Roll <sup>1</sup>	REPE <sup>1</sup>	Pan	Tilt	Roll	REPE	Pan	Tilt	Roll	REPE	Pan	Tilt	Roll	REPE
SL-MH	SL-PB	–	31.11	45.16	83.42	–	12.99	27.13	39.43	–	5.51	12.02	14.89	2.98	<b>3.72</b>	<b>3.63</b>	<b>6.82</b>
	SP360	–	28.91	45.23	82.68	–	12.29	38.42	55.72	–	9.11	37.54	43.56	8.06	<b>8.34</b>	<b>7.77</b>	<b>17.85</b>
	HoliCity	–	33.36	45.20	82.40	–	13.78	45.76	53.99	–	10.94	42.20	47.97	10.74	<b>10.60</b>	<b>8.93</b>	<b>19.84</b>
SL-PB	SL-MH	–	26.92	46.35	76.09	–	11.65	26.50	36.48	–	5.18	13.77	16.99	3.04	<b>3.58</b>	<b>3.39</b>	<b>6.68</b>
	SP360	–	28.29	48.10	78.87	–	12.57	40.25	47.50	–	9.61	40.05	46.07	8.78	<b>8.93</b>	<b>8.28</b>	<b>18.66</b>
	HoliCity	–	32.64	50.37	80.98	–	13.79	46.06	51.72	–	12.53	42.77	49.43	10.95	<b>11.17</b>	<b>9.47</b>	<b>20.62</b>
SP360	SL-MH	–	32.44	47.18	90.97	–	16.25	41.12	49.02	–	8.72	38.96	47.89	6.52	<b>6.82</b>	<b>6.52</b>	<b>15.66</b>
	SL-PB	–	34.31	46.63	90.99	–	16.07	38.38	51.72	–	7.42	37.09	45.45	5.18	<b>5.81</b>	<b>5.60</b>	<b>14.11</b>
	HoliCity	–	30.84	49.19	83.43	–	16.66	44.42	55.47	–	12.83	43.81	51.26	12.65	<b>12.11</b>	<b>10.41</b>	<b>20.48</b>
HoliCity	SL-MH	–	65.52	50.41	96.29	–	14.20	35.44	46.32	–	8.97	33.35	40.48	6.13	<b>6.54</b>	<b>5.97</b>	<b>14.72</b>
	SL-PB	–	65.69	50.95	96.84	–	15.00	47.07	56.54	–	9.59	42.28	49.38	5.26	<b>5.88</b>	<b>5.73</b>	<b>14.85</b>
	SP360	–	64.43	51.59	96.59	–	13.67	42.39	50.36	–	9.43	37.83	43.59	6.10	<b>6.57</b>	<b>6.37</b>	<b>13.31</b>

<sup>1</sup> Units: pan, tilt, and roll [deg]; REPE [pixel]

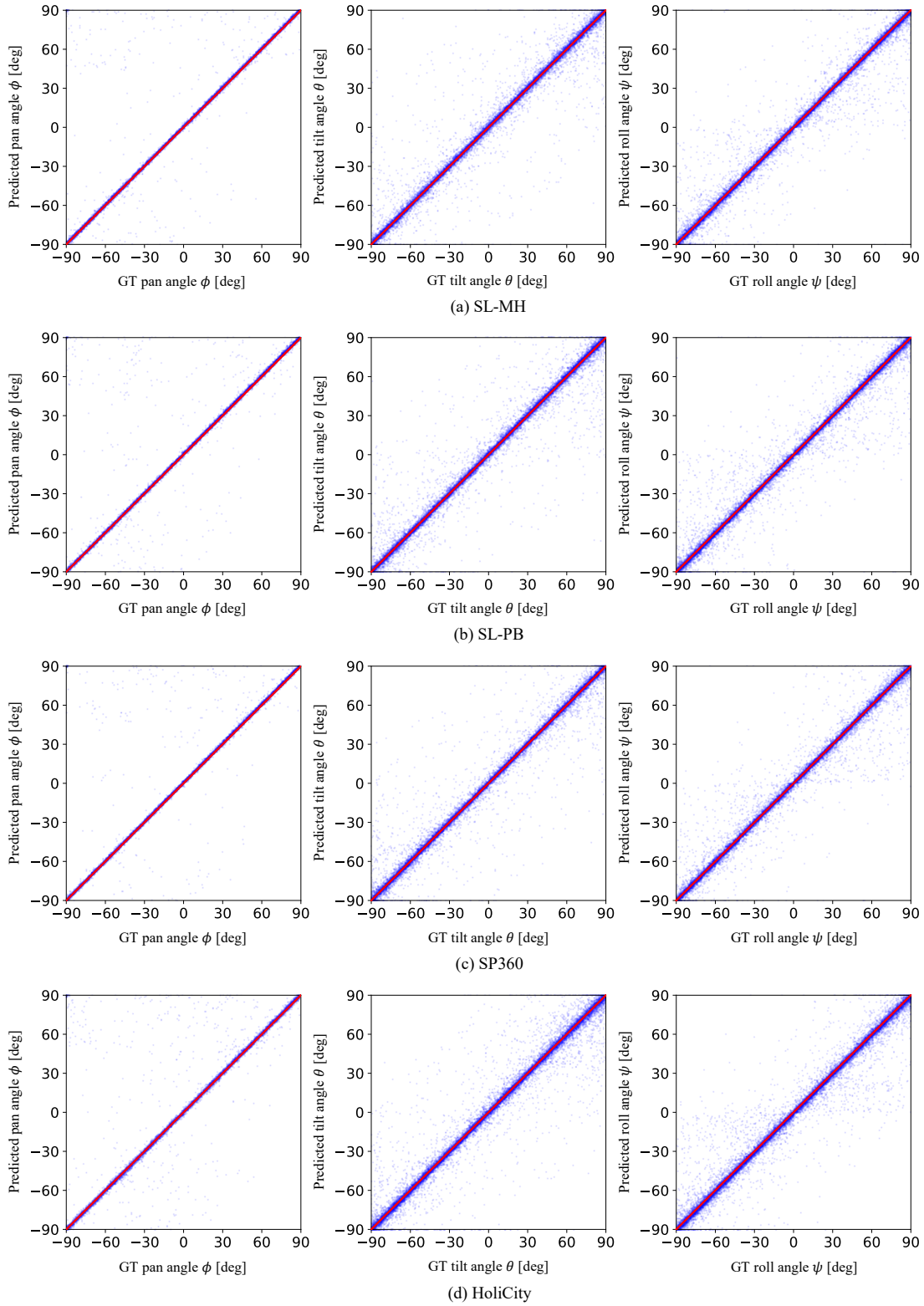


**Figure 11:** Error distribution of angles in our method using HRNet-W32 on the test sets of (a) SL-MH, (b) SL-PB, (c) SP360, and (d) HoliCity. Ground-truth and predicted angles are indicated on the horizontal and vertical axes, respectively. The diagonal red lines represent perfect prediction without angle errors. Each prediction result for the test images is depicted as a translucent blue point.

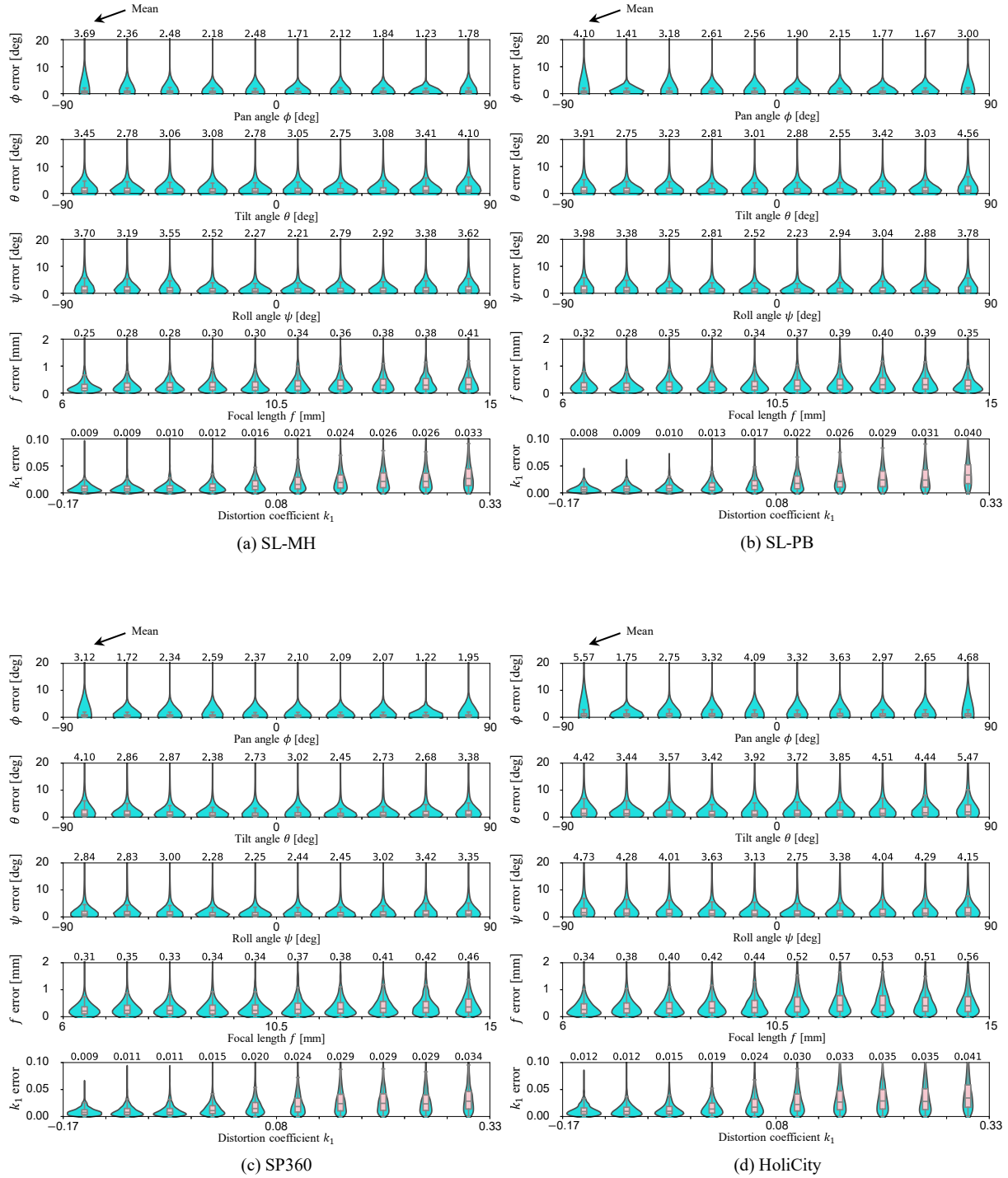


**Figure 12:** Error distribution of our method on the test sets of (a) SL-MH, (b) SL-PB, (c) SP360, and (d) HoliCity. Mean absolute errors are shown in divided ranges as box and violin plots.

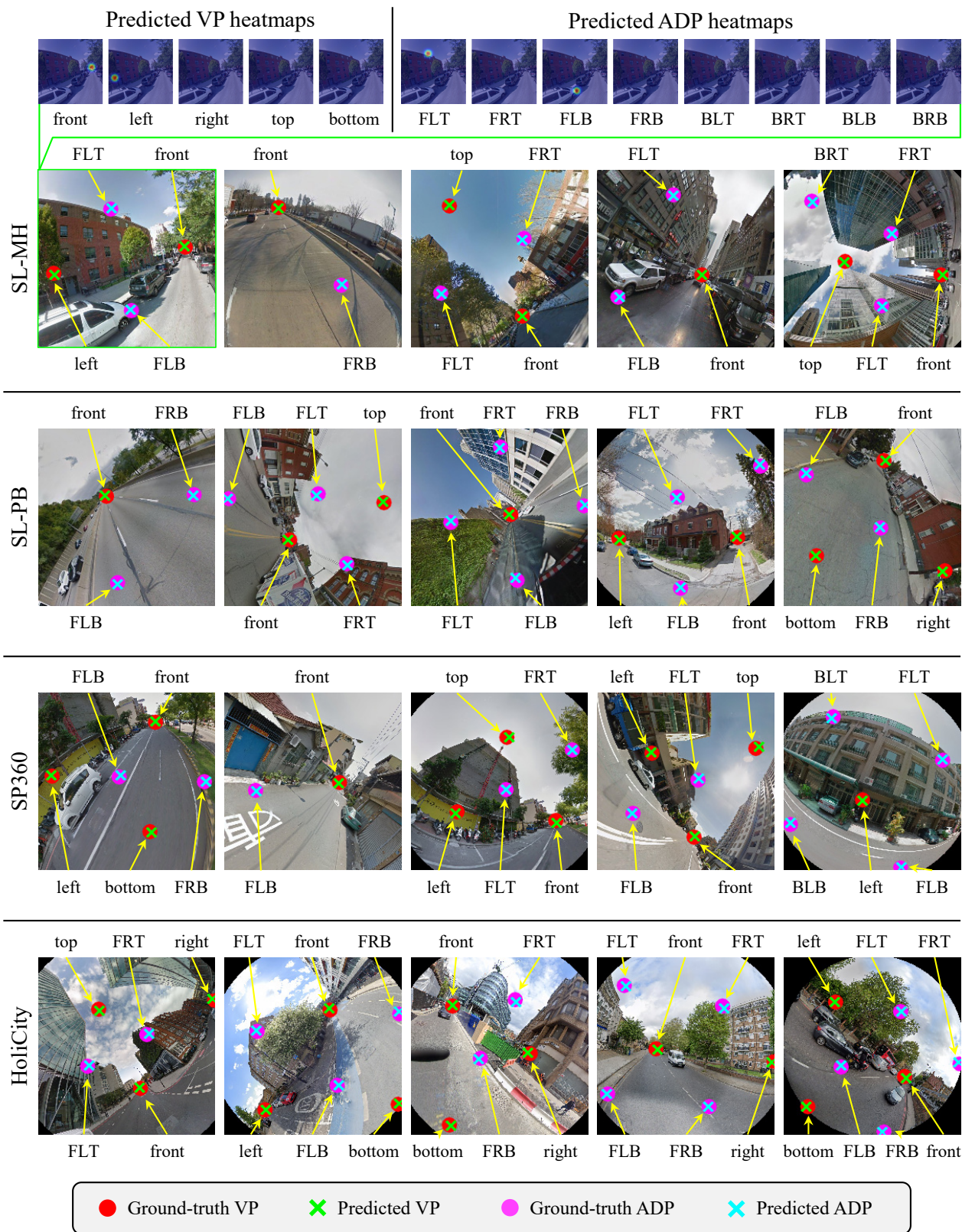
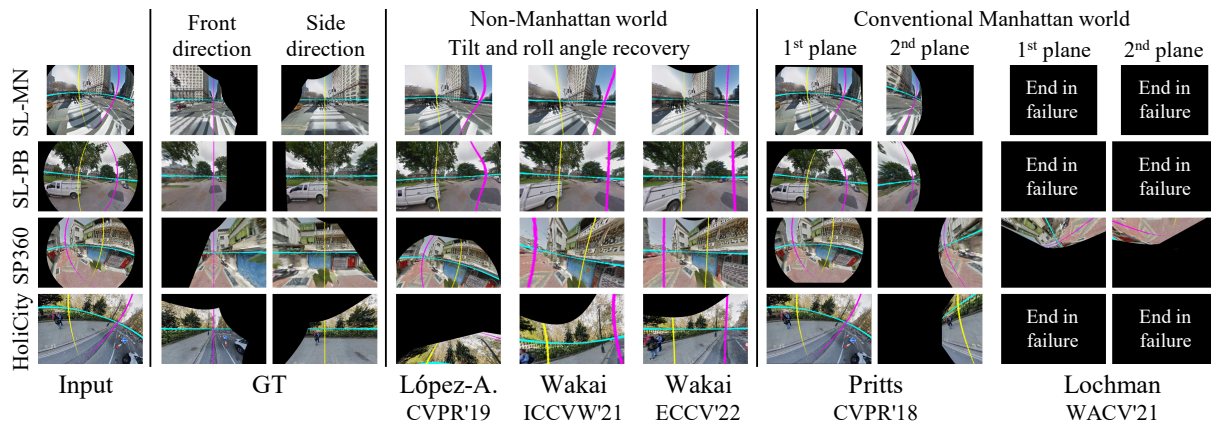
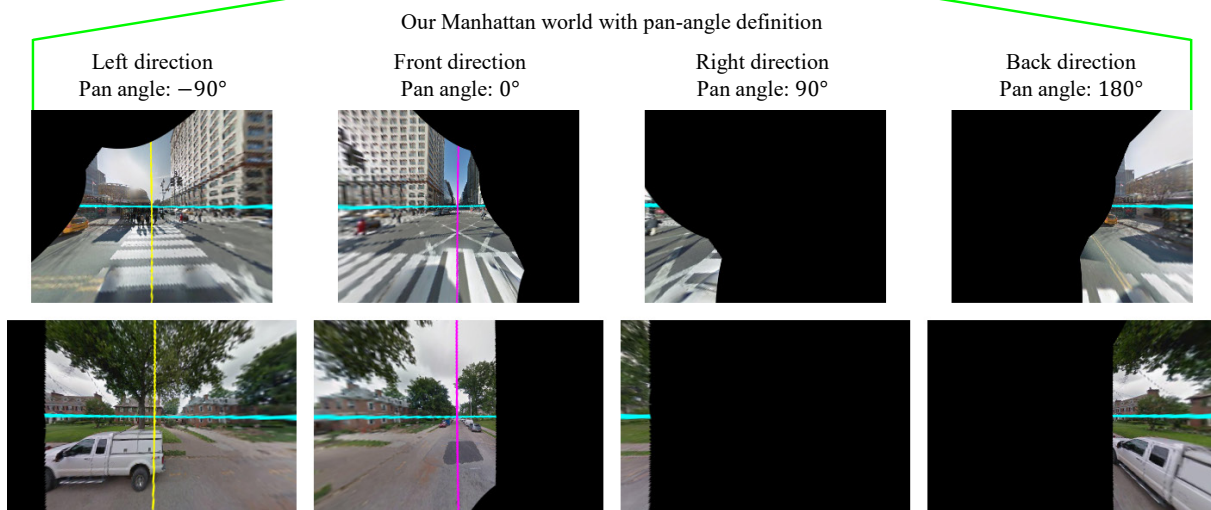
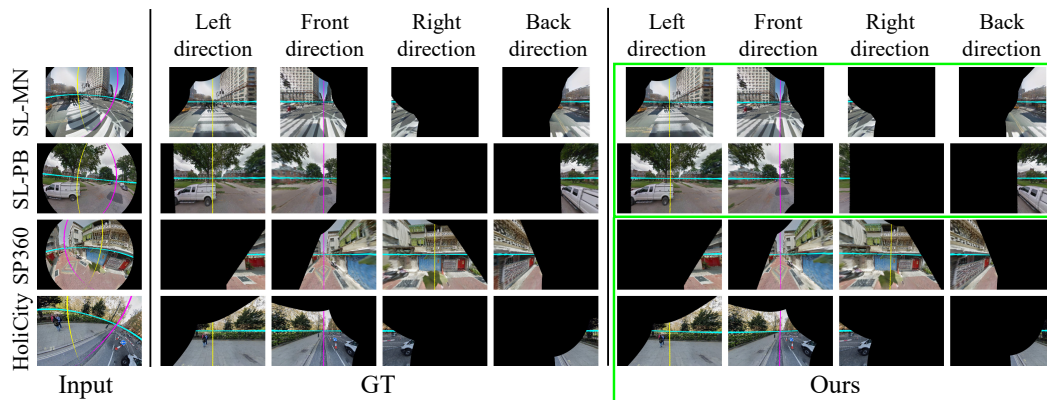


**Figure 13:** Qualitative results of VP/ADP estimation performed by our VP estimator using HRNet-W32 on the test sets of each dataset. The VP/ADP labels correspond to the labels in Table 2.

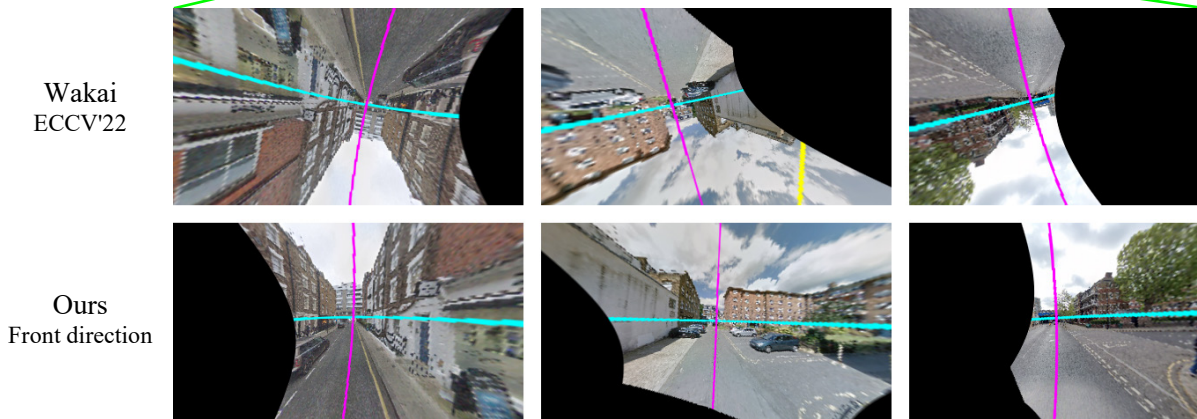
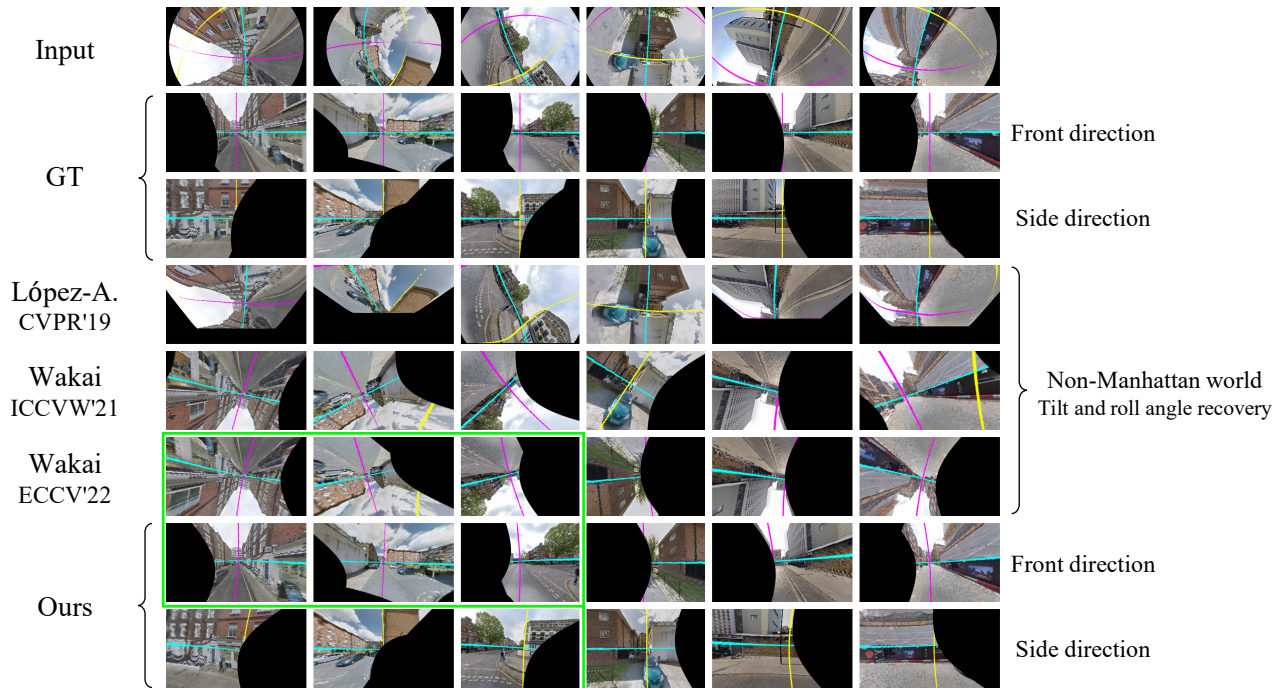


(a) Results of conventional methods



(b) Results of our method

**Figure 14:** Qualitative results on the test sets. (a) Results of conventional methods. From left to right: input images, ground-truth images, and results of López-Antequera [26], Wakai [46], Wakai [45], Pritts [35], and Lochman [25]. (b) Results of our method. From left to right: input images, ground-truth images, and the results of our method in our Manhattan world.



Train: SL-MH, Test: HoliCity

**Figure 15:** Qualitative results in the cross-domain evaluation on the test set of HoliCity. Our method using HRNet-W32 and compared methods were trained on SL-MH. From top to bottom: input images, ground-truth images, and results of López-Antequera [26], Wakai [46], Wakai [45], and our method.

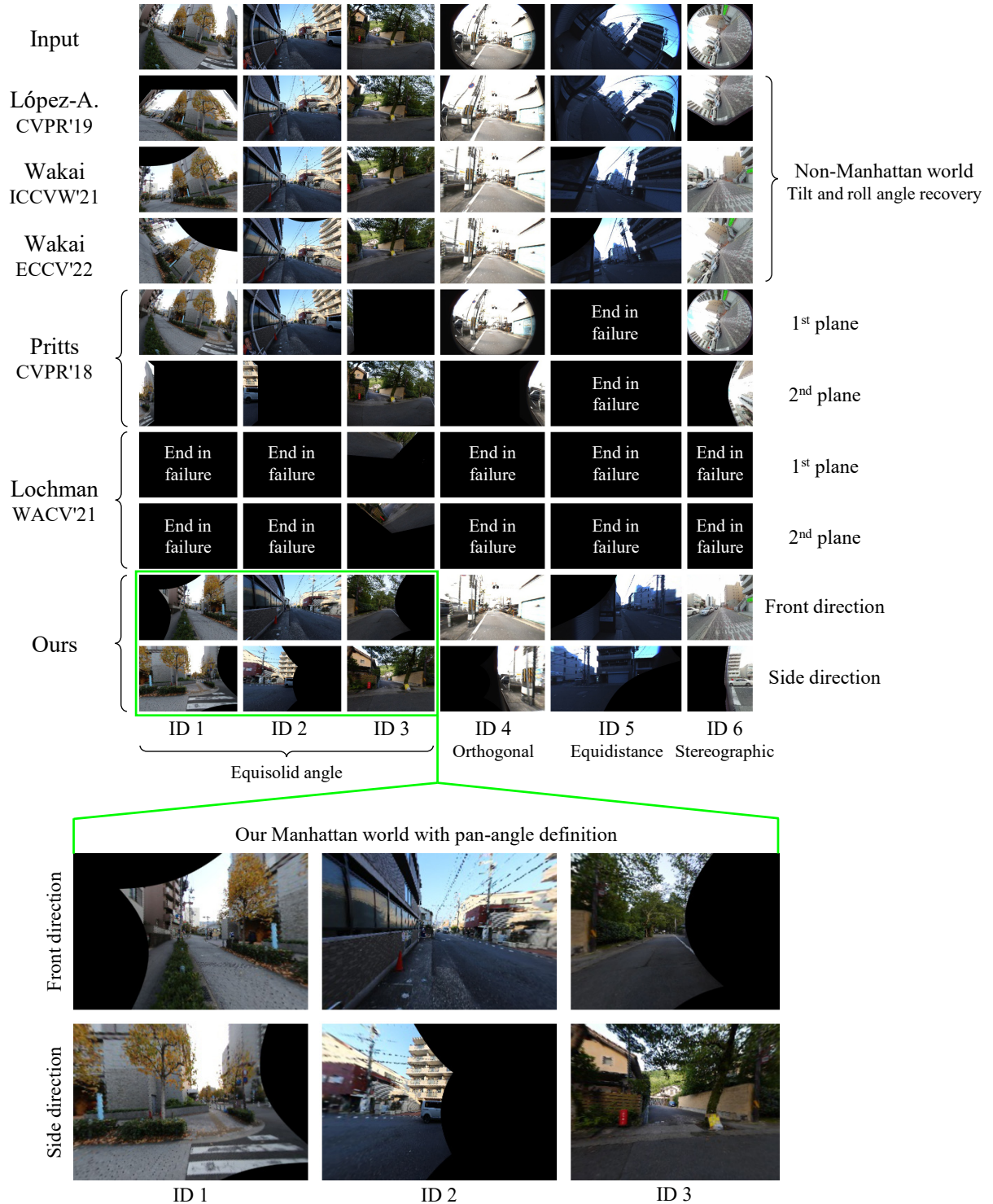


**Figure 16:** Qualitative results for images from off-the-shelf cameras. From top to bottom: input images and results of López-Antequera [26], Wakai [46], Wakai [45], Pritts [35], Lochman [25], and our method. The identifiers (IDs) correspond to the camera IDs used in [45], and the projection names are shown below the IDs.

## References

- [1] M. Andriluka, L. Pishchulin, P. Gehler, and B. Schiele. 2D human pose estimation: New benchmark and state of the art analysis. In *Proceedings of the IEEE Conference on Computer Vision and Pattern Recognition (CVPR)*, pages 3686–3693, 2014. [4](#), [5](#)
- [2] M. Antunes, J. P. Barreto, D. Aouada, and B. Ottersten. Un-supervised vanishing point detection and camera calibration from a single Manhattan image with radial distortion. In *Proceedings of the IEEE Conference on Computer Vision and Pattern Recognition (CVPR)*, pages 6691–6699, 2017. [1](#), [2](#), [3](#), [9](#)
- [3] Z. Cao, G. Hidalgo, T. Simon, S.-E. Wei, and Y. Sheikh. OpenPose: Realtime multi-person 2D pose estimation using part affinity fields. *IEEE Transactions on Pattern Analysis and Machine Intelligence (PAMI)*, 43(1):172–186, 2021. [5](#)
- [4] C.-K. Chang, J. Zhao, and L. Itti. DeepVP: Deep learning for vanishing point detection on 1 million street view images. In *Proceedings of the IEEE International Conference on Robotics and Automation (ICRA)*, pages 4496–4503, 2018. [3](#)
- [5] S. Chang, C. Chiu, C. Chang, K. Chen, C. Yao, R. Lee, and H. Chu. Generating 360 outdoor panorama dataset with reliable sun position estimation. In *Proceedings of the ACM SIGGRAPH Asia*, pages 1–2, 2018. [2](#), [5](#)
- [6] B. Cheng, O. Parkhi, and A. Kirillov. Pointly-supervised instance segmentation. In *Proceedings of the IEEE/CVF Conference on Computer Vision and Pattern Recognition (CVPR)*, pages 2607–2616, 2022. [1](#)
- [7] H.-S. Choi, K. An, and M. Kang. Regression with residual neural network for vanishing point detection. *Image and Vision Computing (IVC)*, 91:103797, 2019. [3](#)
- [8] J. M. Coughlan and A. L. Yuille. Manhattan World: Compass direction from a single image by Bayesian inference. In *Proceedings of the IEEE International Conference on Computer Vision (ICCV)*, volume 2, pages 941–947, 1999. [1](#), [2](#), [3](#)
- [9] A.W. Fitzgibbon. Simultaneous linear estimation of multiple view geometry and lens distortion. In *Proceedings of the IEEE Conference on Computer Vision and Pattern Recognition (CVPR)*, volume 1, pages I–I, 2001. [2](#), [13](#)
- [10] H. Jia, H. Yi, H. Fujiki, H. Zhang, W. Wang, and M. Odamaki. 3D room layout recovery generalizing across Manhattan and non-Manhattan worlds. In *Proceedings of the IEEE/CVF Conference on Computer Vision and Pattern Recognition Workshops (CVPRW)*, pages 5188–5197, 2022. [2](#)
- [11] Y. Kang, Y. Song, W. Ge, and T. Ling. Robust multi-camera SLAM with Manhattan constraint toward automated valet parking. In *Proceedings of the IEEE/RSJ International Conference on Intelligent Robots and Systems (IROS)*, pages 7615–7622, 2021. [2](#), [9](#)
- [12] D. P. Kingma and J. L. Ba. ADAM: A method for stochastic optimization. In *Proceedings of the International Conference on Learning Representations (ICLR)*, 2015. [5](#)
- [13] F. Kluger, H. Ackermann, M. Y. Yang, and B. Rosenhahn. Deep learning for vanishing point detection using an inverse gnomonic projection. In *Proceedings of the German Conference on Pattern Recognition (GCPR)*, pages 17–28, 2017. [3](#)
- [14] F. Kluger, E. Brachmann, H. Ackermann, C. Rother, M. Y. Yang, and B. Rosenhahn. CONSAC: Robust multi-model fitting by conditional sample consensus. In *Proceedings of the IEEE/CVF Conference on Computer Vision and Pattern Recognition (CVPR)*, pages 4634–4643, 2020. [2](#)
- [15] I. Kotseruba, A. Rasouli, and J. K. Tsotsos. Benchmark for evaluating pedestrian action prediction. In *Proceedings of the IEEE/CVF Winter Conference on Applications of Computer Vision (WACV)*, pages 1257–1267, 2021. [1](#)
- [16] J. Lee, H. Go, H. Lee, S. Cho, M. Sung, and J. Kim. CTRL-C: Camera calibration TRansformer with line-classification. In *Proceedings of the IEEE/CVF International Conference on Computer Vision (ICCV)*, pages 16228–16237, 2021. [2](#)
- [17] J. Lee, M. Sung, H. Lee, and J. Kim. Neural geometric parser for single image camera calibration. In *Proceedings of the European Conference on Computer Vision (ECCV)*, pages 541–557, 2020. [2](#)
- [18] H. Li, J. Zhao, J.-C. Bazin, W. Chen, Z. Liu, and Y. Liu. Quasi-globally optimal and efficient vanishing point estimation in Manhattan world. In *Proceedings of the IEEE/CVF International Conference on Computer Vision (ICCV)*, pages 1646–1654, 2019. [2](#)
- [19] K. Li, K. Chen, H. Wang, L. Hong, C. Ye, J. Han, Y. Chen, W. Zhang, C. Xu, D.-Y. Yeung, X. Liang, Z. Li, and H. Xu. CODA: A real-world road corner case dataset for object detection in autonomous driving. In *Proceedings of the European Conference on Computer Vision (ECCV)*, volume 13698, pages 406–423, 2022. [1](#)
- [20] L. Li, T. Zhou, W. Wang, J. Li, and Y. Yang. Deep hierarchical semantic segmentation. In *Proceedings of the IEEE/CVF Conference on Computer Vision and Pattern Recognition (CVPR)*, pages 1236–1247, 2022. [1](#)
- [21] Y.-L. Li and S. Wang. R(Det)<sup>2</sup>: Randomized decision routing for object detection. In *Proceedings of the IEEE/CVF Conference on Computer Vision and Pattern Recognition (CVPR)*, pages 4815–4824, 2022. [1](#)
- [22] Y. Lin, R. Wiersma, S. L. Pintea, K. Hildebrandt, E. Eise-mann, and J. C. van Gemert. Deep vanishing point detection: Geometric priors make dataset variations vanish. In *Proceedings of the IEEE/CVF Conference on Computer Vision and Pattern Recognition (CVPR)*, pages 6093–6103, 2022. [2](#)
- [23] L. Liu, H. Jiang, P. He, W. Chen, X. Liu, J. Gao, and J. Han. On the variance of the adaptive learning rate and beyond. In *Proceedings of the International Conference on Learning Representations (ICLR)*, pages 1–14, 2020. [5](#)
- [24] W. Liu, D. Caruso, E. Ilg, J. Dong, A. I. Mourikis, K. Dani-lidis, V. Kumar, and J. Engel. TLIO: Tight learned inertial odometry. *IEEE Robotics and Automation Letters*, 5(4):5653–5660, 2020. [9](#)
- [25] Y. Lochman, O. Doboševych, R. Hryniv, and J. Pritts. Minimal solvers for single-view lens-distorted camera auto-calibration. In *Proceedings of the IEEE Winter Conference on Applications of Computer Vision (WACV)*, pages 2886–2895, 2021. [1](#), [2](#), [3](#), [6](#), [7](#), [8](#), [9](#), [13](#), [14](#), [15](#), [16](#), [20](#), [22](#)

- [26] M. López-Antequera, R. Marí, P. Gargallo, Y. Kuang, J. Gonzalez-Jimenez, and G. Haro. Deep single image camera calibration with radial distortion. In *Proceedings of the IEEE/CVF Conference on Computer Vision and Pattern Recognition (CVPR)*, pages 11809–11817, 2019. [2](#), [7](#), [8](#), [9](#), [13](#), [14](#), [15](#), [16](#), [20](#), [21](#), [22](#)
- [27] M. Lourakis and G. Terzakis. Efficient absolute orientation revisited. In *Proceedings of the IEEE/RSJ International Conference on Intelligent Robots and Systems (IROS)*, pages 5813–5818, 2018. [5](#), [10](#)
- [28] X. Lu, J. Yao, H. Li, Y. Liu, and X. Zhang. 2-line exhaustive searching for real-time vanishing point estimation in Manhattan world. In *Proceedings of the IEEE Winter Conference on Applications of Computer Vision (WACV)*, pages 345–353, 2017. [2](#)
- [29] K. Ludwig, P. Harzig, and R. Lienhart. Detecting arbitrary intermediate keypoints for human pose estimation with Vision Transformers. In *Proceedings of the IEEE/CVF Winter Conference on Applications of Computer Vision (WACV)*, pages 663–671, 2022. [5](#)
- [30] Z. Luo, Z. Wang, Y. Huang, L. Wang, T. Tan, and E. Zhou. Rethinking the heatmap regression for bottom-up human pose estimation. In *Proceedings of the IEEE/CVF Conference on Computer Vision and Pattern Recognition (CVPR)*, pages 13259–13268, 2021. [4](#)
- [31] Z. Lv, E. Miller, J. Meissner, L. Pesqueira, C. Sweeney, J. Dong, L. Ma, P. Patel, P. Moulon, K. Somasundaram, O. Parkhi, Y. Zou, N. Raina, S. Saariinen, Y. M. Mansour, P.-K. Huang, Z. Wang, A. Troynikov, R. M. Artal, D. DeTone, D. Barnes, E. Argall, A. Lobanovskiy, D. J. Kim, P. Bouttefroy, J. Straub, J. J. Engel, P. Gupta, M. Yan, R. D. Nardi, and R. Newcombe. Aria pilot dataset. <https://about.facebook.com/realitylabs/projectaria/datasets>, 2022. [9](#)
- [32] P. Mirowski, A. Banki-Horvath, K. Anderson, D. Teplyashin, K. M. Hermann, M. Malinowski, M. K. Grimes, K. Simonyan, K. Kavukcuoglu, A. Zisserman, and R. Hadsell. The StreetLearn environment and dataset. *arXiv preprint arXiv:1903.01292*, 2019. [1](#), [2](#), [5](#), [12](#)
- [33] D. Mortari, F. Markley, and P. Singla. Optimal linear attitude estimator. *Journal of Guidance, Control, and Dynamics (JGCD)*, 3:1619–1627, 2007. [5](#), [10](#)
- [34] A. Paszke, S. Gross, F. Massa, A. Lerer, J. Bradbury, G. Chanan, T. Killeen, Z. Lin, N. Gimelshein, L. Antiga, A. Desmaison, A. Kopf, E. Yang, Z. DeVito, M. Raison, A. Tejani, S. Chilamkurthy, B. Steiner, L. Fang, J. Bai, and S. Chintala. PyTorch: An imperative style, high-performance deep learning library. In *Proceedings of the Advances in Neural Information Processing Systems (NeurIPS)*, pages 8024–8035, 2019. [7](#), [14](#)
- [35] J. Pritts, Z. Kukulova, V. Larsson, and O. Chum. Radially-distorted conjugate translations. In *Proceedings of the IEEE/CVF Conference on Computer Vision and Pattern Recognition (CVPR)*, pages 1993–2001, 2018. [1](#), [2](#), [3](#), [6](#), [7](#), [8](#), [9](#), [13](#), [14](#), [15](#), [16](#), [20](#), [22](#)
- [36] O. Russakovsky, J. Deng, H. Su, J. Krause, S. Satheesh, S. Ma, Z. Huang, A. Karpathy, A. Khosla, M. Bernstein, A. C. Berg, and L. Fei-Fei. ImageNet large scale visual recognition challenge. *International Journal of Computer Vision (IJCV)*, 115(3):211–252, 2015. [5](#)
- [37] A. Sheshkus, A. Ingacheva, V. Arlazarov, and D. Nikolaev. HoughNet: Neural network architecture for vanishing points detection. In *Proceedings of the IEEE International Conference on Document Analysis and Recognition (ICDAR)*, pages 844–849, 2019. [3](#)
- [38] Y. Shi, D. Zhang, J. Wen, X. Tong, H. Zhao, X. Ying, and H. Zha. Three orthogonal vanishing points estimation in structured scenes using convolutional neural networks. In *Proceedings of the IEEE International Conference on Image Processing (ICIP)*, pages 3537–3541, 2019. [3](#)
- [39] G. Simon, A. Fond, and M.-O. Berger. A-contrario horizon-first vanishing point detection using second-order grouping laws. In *Proceedings of the European Conference on Computer Vision (ECCV)*, pages 323–338, 2018. [2](#)
- [40] K. Simonyan and A. Zisserman. Very deep convolutional networks for large-scale image recognition. In *Proceedings of the International Conference on Learning Representations (ICLR)*, 2015. [13](#)
- [41] K. Sun, B. Xiao, D. Liu, and J. Wang. Deep high-resolution representation learning for human pose estimation. In *Proceedings of the IEEE/CVF Conference on Computer Vision and Pattern Recognition (CVPR)*, pages 5686–5696, 2019. [4](#), [5](#), [13](#), [14](#), [15](#)
- [42] J.-P. Tardif. Non-iterative approach for fast and accurate vanishing point detection. In *Proceedings of the IEEE International Conference on Computer Vision (ICCV)*, pages 1250–1257, 2009. [2](#)
- [43] X. Tong, X. Ying, Y. Shi, R. Wang, and J. Yang. Transformer based line segment classifier with image context for real-time vanishing point detection in Manhattan world. In *Proceedings of the IEEE/CVF Conference on Computer Vision and Pattern Recognition (CVPR)*, pages 6083–6092, 2022. [2](#)
- [44] T.-D. Truong, Q.-H. Bui, C. N. Duong, H.-S. Seo, S. L. Phung, X. Li, and K. Luu. DirecFormer: A directed attention in Transformer approach to robust action recognition. In *Proceedings of the IEEE/CVF Conference on Computer Vision and Pattern Recognition (CVPR)*, pages 19998–20008, 2022. [1](#)
- [45] N. Wakai, Y. Ishii, S. Sato, and T. Yamashita. Rethinking generic camera models for deep single image camera calibration to recover rotation and fisheye distortion. In *Proceedings of the European Conference on Computer Vision (ECCV)*, volume 13678, pages 679–698, 2022. [2](#), [3](#), [4](#), [5](#), [6](#), [7](#), [8](#), [9](#), [12](#), [13](#), [14](#), [15](#), [16](#), [20](#), [21](#), [22](#)
- [46] N. Wakai and T. Yamashita. Deep single fisheye image camera calibration for over 180-degree projection of field of view. In *Proceedings of the IEEE/CVF International Conference on Computer Vision Workshops (ICCVW)*, pages 1174–1183, 2021. [2](#), [7](#), [8](#), [9](#), [13](#), [14](#), [15](#), [16](#), [20](#), [21](#), [22](#)
- [47] Z. Wang and A. C. Bovik. Image quality assessment: From error visibility to structural similarity. *IEEE Transactions on Image Processing (TIP)*, 13(4):600–612, 2004. [13](#)
- [48] Z. Wang and Jepson. A new closed-form solution for absolute orientation. In *Proceedings of the IEEE Conference*

- on *Computer Vision and Pattern Recognition (CVPR)*, pages 129–134, 1994. 4, 9
- [49] H. Wildenauer and B. Micusik. Closed form solution for radial distortion estimation from a single vanishing point. In *Proceedings of the British Machine Vision Conference (BMVC)*, pages 106.1–106.11, 2013. 1, 2, 3, 9
- [50] J. Wu, L. Zhang, Y. Liu, and L. Chen. Real-time vanishing point detector integrating under-parameterized RANSAC and Hough transform. In *Proceedings of the IEEE/CVF International Conference on Computer Vision (ICCV)*, pages 3712–3721, 2021. 2
- [51] J. Yang, X. Dong, L. Liu, C. Zhang, J. Shen, and D. Yu. Recurring the Transformer for video action recognition. In *Proceedings of the IEEE/CVF Conference on Computer Vision and Pattern Recognition (CVPR)*, pages 14043–14053, 2022. 1
- [52] R. Yunus, Y. Li, and F. Tombari. ManhattanSLAM: Robust planar tracking and mapping leveraging mixture of Manhattan frames. In *Proceedings of the IEEE International Conference on Robotics and Automation (ICRA)*, pages 6687–6693, 2021. 2, 9
- [53] M. Zhai, S. Workman, and N. Jacobs. Detecting vanishing points using global image context in a non-Manhattan world. In *Proceedings of the IEEE Conference on Computer Vision and Pattern Recognition (CVPR)*, pages 5657–5665, 2016. 3
- [54] F. Zhang, X. Zhu and H. Dai, M. Ye, and C. Zhu. Distribution-aware coordinate representation for human pose estimation. In *Proceedings of the IEEE/CVF Conference on Computer Vision and Pattern Recognition (CVPR)*, pages 7091–7100, 2020. 4
- [55] T. Zheng, Y. Huang, Y. Liu, W. Tang, and Z. Yang. CLRNet: Cross layer refinement network for lane detection. In *Proceedings of the IEEE/CVF Conference on Computer Vision and Pattern Recognition (CVPR)*, pages 888–897, 2022. 1
- [56] Z. Zhong, L. Zheng, G. Kang, S. Li, and Y. Yang. Random Erasing data augmentation. In *Proceedings of the AAAI Conference on Artificial Intelligence*, 2020. 5
- [57] Y. Zhou, J. Huang, X. Dai, L. Luo, Z. Chen, and Y. Ma. HoliCity: A city-scale data platform for learning holistic 3D structures. *arXiv preprint arXiv:2008.03286*, 2020. 2, 5
- [58] Y. Zhou, H. Qi, J. Huang, and Y. Ma. NeurVPS: Neural vanishing point scanning via conic convolution. In *Proceedings of the Advances in Neural Information Processing Systems (NeurIPS)*, 2019. 2